Spectroscopic determination of the intermolecular potential energy surface for Ar–NH_3

C. A. Schmuttenmaer,[a] R. C. Cohen,[b] and R. J. Saykally
Department of Chemistry, University of California, Berkeley, California 94720

(Received 15 November 1993; accepted 23 March 1994)

The three-dimensional intermolecular potential energy surface (IPS) for Ar–NH_3 has been determined from a least-squares fit to 61 far infrared and microwave vibration–rotation–tunneling (VRT) measurements and to temperature-dependent second virial coefficients. The three intermolecular coordinates (R, θ, ϕ) are treated without invoking any approximations regarding their separability, and the NH_3 inversion–tunneling motion is included adiabatically. A surface with 13 variable parameters has been optimized to accurately reproduce the spectroscopic observables, using the collocation method to treat the coupled multidimensional dynamics within a scattering formalism. Anisotropy in the IPS is found to significantly mix the free rotor basis functions. The 149.6 cm^{-1} global minimum on this surface occurs with the NH_3 symmetry axis nearly perpendicular to the van der Waals bond axis (θ=96.6°), at a center-of-mass separation of 3.57 Å, and with the Ar atom midway between two of the NH_3 hydrogen atoms (ϕ=60°). The position of the global minimum is very different from the center-of-mass distance extracted from microwave spectroscopic studies. Long-range (R>3.8 Å) attractive interactions are greatest when either a N–H bond or the NH_3 lone pair is directed toward the argon. Comparisons with *ab initio* surfaces for this molecule as well as the experimentally determined IPS for Ar–H_2O are presented.

I. INTRODUCTION

The ultimate goal of spectroscopic investigations of weakly bound complexes (WBCs) is to quantitatively characterize the intermolecular forces and the associated multidimensional internal dynamics that operate in these systems. It has been shown in recent work[1] that even for simple binary clusters such as Ar–HCl and Ar–H_2O, it is misleading to treat the dynamics by approximate methods (e.g., reversed adiabatic approximation) which reduce the dimensionality of the problem. Moreover, a very detailed mathematical form must be employed to represent the intermolecular potential energy surface (IPS), if spectroscopic accuracy is to be reproduced. As a consequence, the problem of determining the complete IPS from spectroscopic data is a difficult one, limited both by available computing resources and by theoretical methods for accurately calculating bound state properties from multidimensional IPS. Of necessity, such calculations must proceed via a scattering formalism due to the coupled large amplitude motions that characterize WBCs. The state-of-the-art for IPS determination currently extends only to three-dimensional systems. Le Roy and co-workers have extensively studied the rare gas–H_2 (Rg–H_2) complexes,[2] and Hutson has determined detailed IPS for several binary Rg–hydrogen halide (HX) complexes, explicitly including the dependence on diatomic bond length.[3,4] Cohen and Saykally have determined the 3D IPS for the interaction of ground state water molecules with argon by the use of the collocation method.[1,5] In this paper we extend this list to the quasi four-dimensional Ar–NH_3 system, using collocation to solve the close-coupled scattering Hamiltonian with spectroscopic accuracy.

Of course, it is hoped that these detailed and accurate IPS will be useful both for extracting a general description of intermolecular forces and for enhancing our capabilities to model liquids and solids. However, in the latter context, their mathematical forms are somewhat too complicated to be employed directly in current computer simulations. We should instead regard them as benchmarks for testing both simplified empirical IPS and *ab initio* methods, which are in turn, widely used in molecular modeling. It is important to recognize that the regions of the IPS sampled by WBCs are directly relevant to the structures of liquids. For example, in liquid water at densities of 1 g/cm^3, the most probable nearest-neighbor distance between molecules is 2.9 Å,[6] whereas the equilibrium center-of-mass separation in the gaseous water dimer has been determined to be about 3.0 Å.[7] For liquid ammonia, x-ray diffraction data indicate that the most probable nearest-neighbor distance is 3.4 Å,[8] while the gas phase separation in $(NH_3)_2$ is near 3.4 Å[9] and that for Ar–NH_3 is near 3.6 Å. Thus the interaction distances in these liquids are quite similar to those in gaseous dimers studied by spectroscopic methods, and IPS determined from these data characterize the molecular interactions over the appropriate distance ranges.

The work presented here is the first experimental determination of the multidimensional IPS of the Ar–NH_3 dimer. To date, three levels of sophistication have been applied with respect to gaining physical insight into the IPS of weakly bound dimers through analysis of spectroscopic observables. The first is a strictly phenomenological approach, wherein molecular constants are determined by fitting the observed transitions to standard energy level expressions.[10] From these constants, one can make arguments as to which bands are

[a]Present address: Department of Chemistry, University of Rochester, Rochester, NY 14627.
[b]Present address: Department of Chemistry, Harvard University, Cambridge, MA 02138.

 0021-9606/94/101(1)/146/28/$6.00

stretching or bending vibrations—if there are no major perturbations. Furthermore, the extent of Coriolis interaction between two (or more) states can sometimes be determined. The next highest level of sophistication is to determine an effective angular IPS for the complex.[11,12] This is a reasonable treatment for complexes with subunits that undergo nearly free internal rotation, but as shown by Cohen *et al.* for Ar–H_2O, it does not correctly describe the dynamics of systems possessing even moderate angular-radial coupling. The highest level of sophistication is to determine the complete intermolecular potential energy surface. Given this information, one can unequivocally ascertain the nature of the intermolecular vibrations and the interactions among the different motions. Such a determination constitutes the subject of this paper.

A. Ar–NH_3: Nomenclature and background

The work presented here involves the lowest two inversion–tunneling states of NH_3, viz. the symmetric and antisymmetric states with $v_2=0$. The quantum number for the inversion–tunneling state will be designated by v, where $v=0$ is the symmetric state, and $v=1$ is the antisymmetric state. The vdW states are labeled with quantum numbers describing the free internal rotor level that a given vibration–rotation–tunneling (VRT) state most nearly correlates with. The VRT states are reasonably pure at low energies, but with as little as 30 cm^{-1} of excitation, many of them are highly mixed, and might have less than 60% character of any single free rotor basis state. Nonetheless, these labels provide a convenient means to discuss the states. The relevant quantum numbers are: a capital Greek letter ($\Sigma,\Pi,\Delta,...$) indicating the amount of angular momentum projected on the vdW axis, the quantum numbers (j_k) of the free rotor state of the NH_3 monomer that the state of the complex most nearly correlates with, and finally the number of quanta of vdW stretch (n).

Additional qualifiers are necessary for states in which $k\neq 0$ since the nuclear spin-allowed free rotor states are then doubled due to inversion tunneling of NH_3. Upon inversion of the NH_3 subunit, $\theta\rightarrow\pi-\theta$, where θ is the angle between the NH_3 symmetry axis and the vdW bond axis. In Σ states with $k\neq 0$, the potential energy surface along the inversion–tunneling coordinate remains nearly symmetric since these wave functions are nearly symmetric (or antisymmetric) with respect to 90° in the θ coordinate, i.e., there is about the same probability of finding the complex with θ as with $\pi-\theta$. Therefore, it is found that the Σ states come in pairs of opposite parity, separated by roughly the unperturbed inversion splitting of NH_3 (24 GHz). The additional qualifiers are then an "s" or "a" superscript for Σ states, with s designating symmetric and a designating an antisymmetric NH_3 monomer inversion wave function. States with $k\neq 0$ in which there is a nonzero projection of angular momentum onto the vdW axis behave quite differently, however. In these states, the wave functions are not symmetric about $\theta=90°$, which implies that the NH_3 is in an asymmetric environment along the inversion coordinate. The inversion is thus quenched, resulting in two states whose energy separation is approximated by the average difference in energy of the two wells of the effective asymmetric inversion potential. This relatively large splitting occurs for both parities, and the result is two sets of nearly degenerate parity doublets with several wave numbers difference in energy between the sets. For $k\neq 0$ states possessing angular momentum on the vdW axis, superscripts of "upper" and "lower" designate which pair of nearly degenerate levels is higher in energy. Thus, the designation $\Pi(1_0,\ n=0)$ refers to the state that correlates to $j_k=1_0$, has one unit of angular momentum projected on the vdW axis, and zero quanta of vdW stretch excited, while the designation $\Delta^{\text{upper}}(2_1,\ n=0)$ refers to the higher energy state of the two that most nearly correlate to $j_k=2_1$, have two units of angular momenta projected on the vdW axis, and have zero quanta of vdW stretch excited.

The first studies of Ar–NH_3 were done in the microwave region[13,14] where $(B+C)/2$ (the pseudodiatomic rotational constant), dipole moment, and quadrupole coupling constant of the ground state of the dimer were determined. In addition to the assigned lines, many transitions were observed near 20 GHz and attributed to tunneling transitions. It was not until several years later that these transitions were definitely assigned to tunneling transitions in the E states of Ar–NH_3.[12]

There has been a large amount of FIR and submillimeter work done on this molecule, and the results of these studies provide the most valuable information needed to accurately determine the IPS. In 1990 Gwo *et al.* reported a bending vibration at 26.5 cm^{-1} which correlated to $j_k=1_0\leftarrow j_k=0_0$.[10] In 1991 Zwart *et al.* assigned the transitions among the E states correlating to $j_k=1_1$.[12] Their work demonstrated unambiguously that there are some states in which the NH_3 subunit is nearly freely inverting. Also in 1991 Schmuttenmaer *et al.* reported two more FIR bands—one bend and the vdW stretch.[11] Most recently, Schmuttenmaer *et al.*[15] have measured eight more states, including the four states correlating to $j_k=1_1$ with one quantum of vdW stretch excited, and two states that correlate to $j_k=2_1$, and Grushow *et al.*[16] have measured the other four states that correlate to $j_k=2_1$. The spectroscopic measurement and subsequent assignment of these 12 higher energy states has been critical to the determination of the IPS.

Two relevant nonspectroscopic studies of Ar–NH_3 have been reported as well. Schleipen *et al.* have measured the state to state cross sections for rotational excitation of *ortho* and *para* NH_3 by Ar.[17] These cross sections are particularly sensitive to the anisotropy in the repulsive portion of the IPS. Since the spectroscopic data are ostensibly less sensitive to the repulsive region of the IPS than the scattering data, a comparison of their experimental cross sections with those calculated from the IPS determined from our work will be a stringent test of shape of the repulsive wall. The second relevant nonspectroscopic study is the measurement of the second virial coefficients by Schramm *et al.*,[18] which help to determine the isotropically averaged well depth.

There has also been a considerable amount of theoretical effort directed toward Ar–NH_3. Chałasiński *et al.*[19] published an *ab initio* study in 1989 in which the NH_3 subunit was fixed at its equilibrium geometry, and found the global minimum to be 115 cm^{-1} deep, located at $R=3.76$ Å, $\theta=101°$, and $\phi=60°$. In 1991, Bulski *et al.* determined four *ab initio* IPS, each for different umbrella angles of the NH_3

subunit.[20] Their surface with the NH_3 subunit fixed at its equilibrium structure placed the 134 cm^{-1} deep global minimum at $R=3.59$ Å, $\theta=105°$, and $\phi=60°$. These two *ab initio* studies are compared with each other and with the experimentally determined IPS in Sec. IV B. The bound rovibrational states and a vibration–rotation–inversion spectrum of Ar–NH_3 with the NH_3 subunit in its equilibrium position were calculated by van Bladel *et al.*[21,22] in 1991. They used the *ab initio* IPS of Bulski *et al.*, and found that better agreement with experiment was obtained when scaling the repulsive contribution to the $V_{33}(R)$ parameter by a factor of 1.43. Later in 1991, Schmuttenmaer *et al.*[11] and Zwart *et al.*[12] each determined an effective angular IPS from their experimental data. These two surfaces are in close agreement, even though Schmuttenmaer *et al.* determined their surface from data for the *ortho* states, while Zwart *et al.* used data from *para* states. This gave encouragement that the surfaces were essentially correct, within the limitations imposed by not treating the radial coordinate explicitly.

In 1992, van Bladel *et al.*[23] calculated the rovibrational states of Ar–NH_3 again using the scaled *ab initio* IPS of Bulski *et al.* except that this time they explicitly included the umbrella inversion coordinate of the NH_3 subunit. They found that the model previously used[21] wherein the NH_3 inversion tunneling is treated adiabatically was valid for the ground vibrational state. Based on their success, we employ the adiabatic model to describe the NH_3 inversion tunneling in the present work.

In 1992, van der Sanden *et al.*[24] calculated the rotational excitation cross sections of NH_3 by Ar measured by Schleipen *et al.*[17] They used the *ab initio* surface of Bulski *et al.*, both with and without scaling the $V_{33}(R)$ coefficient and treated the NH_3 inversion tunneling by both adiabatically and explicitly including the inversion coordinate. They found the best agreement with experiment when using the scaled *ab initio* potential, and they found that treating the inversion tunneling adiabatically did not significantly degrade the agreement with experiment.

The IPS determined in this work places the 149.6 cm^{-1} deep global minimum at $R=3.57$ Å, $\theta=96.6°$, and $\phi=60°$. This is a nearly T-shaped configuration, with the Ar atom midway between two hydrogens. The *ab initio* results are in reasonable agreement with this IPS.

II. COMPUTATIONAL ASPECTS

A. Background

We choose a form for the IPS that explicitly treats motions of the subunits relative to each other, yet averages over the high-frequency vibrations of the monomers themselves. Thus, a different IPS will be obtained for each monomer vibrational state; in this work we will determine the IPS for the ground vibrational state of NH_3. The IPS is determined by iteratively solving the Schrödinger equation using a trial IPS and comparing experimental observables with calculated ones until one is found that satisfactorily reproduces all the data in the sense of minimum rms deviation.

There are, of course, many ways to solve the time-independent Schrödinger equation; we chose the collocation method[5,25–27] for three reasons. First, it has been shown that the results are as accurate as a variational solution using the same size basis.[25] Second, it has the advantage over a variational approach that no integrals need be evaluated. This affords a savings in computer time that ultimately translates into being able to incorporate the calculation of eigenvalues and eigenvectors in a nonlinear least-squares routine to fit the IPS. Third, both eigenvectors and eigenvalues are obtained so properties that are determined from the wave functions, such as dipole moments and quadrupole coupling constants, can be calculated directly. This is in contrast to the close-coupling approach advocated by Hutson, in which these properties are obtained via finite difference methods.[28]

The successful application of the collocation method to molecular bound state systems was first demonstrated by Yang and Peet in 1988 when they solved the Morse oscillator problem using this method.[25] Next, they solved the Ar–HCl system first with $J=0$,[26] and then with $J>0$,[27] and showed that their results were as accurate as a variational calculation with numerical integration with the same number of points, yet their calculation took only a fraction of the time. Subsequently, Cohen *et al.* applied the collocation method to the three-dimensional system, Ar–H_2O.[1,5] A significant aspect of that work is that the eigenstate calculation was incorporated in a nonlinear least-squares loop in order to fit a IPS from experimental data. It was the computational efficiency of the method that allowed this to be done. Here we present the determination of the 3D IPS of an atom—symmetric top complex, Ar–NH_3, by iteratively fitting the IPS to FIR and microwave experimental data, and explicitly including the NH_3 inversion as a fourth degree of freedom in the dynamics.

The most obvious differences between this work and the Ar–H_2O study is in the symmetry of the monomer, C_{2v} for H_2O vs D_{3h} for NH_3 and the fact that inversion tunneling is present in NH_3. Conceptually, our approach consists of two parts, the calculation of the observables and the comparison of these observables with actual experimental data. This is repeated until a IPS is obtained that yields the experimental data to a desired accuracy. The majority of the time (94%) is spent calculating the observables, i.e., diagonalizing the Hamiltonian matrix, even when using the expedient collocation method.

B. The coordinate system and Hamiltonian

The Ar–NH_3 complex is described with a body-fixed Jacobi coordinate system with the origin at the NH_3 center of mass. The positive Z axis is collinear with the vector $\mathbf{R}$ of length R, which is defined to point from the origin to the Ar atom. The coordinate system for the NH_3 monomer also has the origin at the NH_3 center of mass. It is given by z' along the threefold symmetry axis, and the positive direction is defined to point from the nitrogen atom to the plane of the hydrogens, thus making the dipole moment positive. One of the hydrogens lies in the $x'z'$ plane, along the $+x'$ direction, thereby defining the x' and y' axes. The orientation of the coordinate system of the monomer (x',y',z') relative to the body-fixed system (X,Y,Z) is defined by the Euler angles γ, θ, ϕ: γ is the azimuthal angle of the z' axis in the X, Y, Z

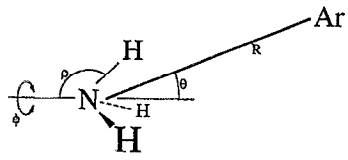

FIG. 1. The Ar–NH_3 coordinate system. The distance from the Ar atom to the NH_3 center of mass is denoted R. The angle between the symmetry axis of NH_3 and R is denoted θ, and ϕ is the amount of rotation of NH_3 about its symmetry axis. The NH_3 monomer inversion-tunneling coordinate is ρ.

coordinate system, θ is the angle between Z and z', the symmetry axis of NH_3 and $\mathbf{R}$, respectively, and ϕ specifies the degree of rotation of NH_3 about its symmetry axis. Thus, $\theta=0°$ describes the complex in an Ar–H_3N orientation, and $\theta=180°$ depicts an Ar–NH_3 orientation. Furthermore, when $\phi=0°$, the argon, nitrogen, and the hydrogen atom closest to the Ar are all coplanar, whereas the Ar will lie in between two hydrogens when $\phi=60°$. The interaction energy of the Ar and NH_3 is independent of γ, the azimuthal angle of the z' axis. Finally, the coordinate for describing the umbrella vibration in NH_3, ρ, is considered. We will employ the convention chosen by van Bladel *et al.* for the inversion–tunneling coordinate as the angle of an N–H bond relative to the C_3 symmetry axis.[23] It is important to note that ρ and θ are related to each other, namely, that upon inversion $\rho\rightarrow\pi-\rho$ and $\theta\rightarrow\pi-\theta$. Figure 1 presents the coordinate system.

It is assumed that the inversion–tunneling motion of the NH_3 subunit can be treated adiabatically. The validity of this assumption has been discussed in Refs. 21, 23, and 24, and a summary of their argument follows. There are two motions of very different time scales along the inversion coordinate of NH_3. One is the high-frequency umbrella vibration at roughly 950 cm^{-1} that is localized in one-half of the double well. This motion, just like the other high-frequency monomer modes, is much faster than the intermolecular vdW motions. Therefore, we are justified in using a vibrationally averaged structure for the NH_3 monomer, and in neglecting coupling to the high-frequency modes. The second motion involving this coordinate is the inversion tunneling itself. The inversion frequency in the ground state of NH_3 ($\Delta\approx0.8$ cm^{-1}) is considerably lower than that of the vdW motions, which are closer to 20 cm^{-1}, so there should also be minimal coupling between these types of motions. We may then treat the inversion in the complex by including both inversion states of the monomer functions in the basis. Van Bladel *et al.*[23] find that in the ground vibrational state, the energy levels calculated using this model are accurate to 0.01 cm^{-1} (300 MHz), and the inversion–tunneling splittings are accurate to 10^{-4} cm^{-1} (3 MHz).

The Hamiltonian for Ar–NH_3 is

$$\hat{H}=-\frac{\hbar^2}{2\mu R^2}\frac{\partial^2}{\partial R^2}R+\frac{\hbar^2}{2\mu R^2}(\hat{J}^2+\hat{j}^2-2\hat{j}\cdot\hat{J})+\hat{H}_{\text{mon}}+V(R,\theta,\phi), \quad (1)$$

where

TABLE I. Molecular parameters used in the determination of the Ar–NH_3 intermolecular IPS.

Molecule	Constant	Value	Reference
Ar	α	$11.096a_0^3$	29
NH_3	μ	$0.57892\ ea_0$	30
	Θ	$-1.725\ ea_0^2$	31
	Ω_{30}	$-1.69\ ea_0^3$	31
	Ω_{33}	$-1.72\ ea_0^3$	31
	Ω^a	$2.96\ ea_0^3$	31
	$B^{(0)}$	9.946 6422 cm^{-1}	32
	$C^{(0)}-B^{(0)}$	−3.719 9204 cm^{-1}	32
	$D_J^{(0)}$	$0.849\,393\times10^{-3}$ cm^{-1}	32
	$D_{JK}^{(0)}$	$-1.577\,73\times10^{-3}$ cm^{-1}	32
	$D_K^{(0)}$	$0.810\,18\times10^{-3}$ cm^{-1}	32
	$B^{(1)}$	9.941 5887 cm^{-1}	32
	$C^{(1)}-B^{(1)}$	−3.712 8676 cm^{-1}	32
	$D_J^{(1)}$	$0.832\,605\times10^{-3}$ cm^{-1}	32
	$D_{JK}^{(1)}$	$-1.531\,40\times10^{-3}$ cm^{-1}	32
	$D_K^{(1)}$	$0.778\,43\times10^{-3}$ cm^{-1}	32
	Δ	0.793 4083 cm^{-1}	32
ND_3	B	5.138 cm^{-1}	33
	$C-B$	−1.981 cm^{-1}	33
	Δ	1600 MHz	33
Ar–NH_3	Reduced mass	11.943 317 amu	
Ar–ND_3	Reduced mass	13.353 51 amu	
Dispersion coefficients	C_6^{00}	71.216 a.u.	34
	C_6^{20}	−0.160 a.u.	34
	C_7^{10}	61.026 a.u.	34
	C_7^{30}	−22.659 a.u.	34
	C_7^{33}	−29.776 a.u.	34
Induction coefficients	C_6^{00}	$\alpha\mu^2$	11
	C_6^{20}	$\alpha\mu^2$	11
	C_7^{10}	$(18/5)\alpha\mu\Theta$	11
	C_7^{30}	$(12/5)\alpha\mu\Theta$	11

[a]$\Omega^2=\Omega_{30}^2+2\Omega_{33}^2$.

$$\hat{H}_{\text{mon}}=B_x\hat{j}_x^2+B_y\hat{j}_y^2+B_z\hat{j}_z^2+\hat{H}_{\text{inv}} \quad (2)$$

and $\hat{j}_x$, $\hat{j}_y$, and $\hat{j}_z$ are the angular momentum operators in the Cartesian frame of the monomer, and $\hat{H}_{\text{inv}}$ is the inversion Hamiltonian for NH_3. The energy level expression for the monomer rotation–inversion levels (which constitute the zero-order bending vibrational levels of the complex) is

$$E(j,k,v)=B^{(v)}j(j+1)+(C^{(v)}-B^{(v)})k^2-D_J^{(v)}j^2(j+1)^2-D_{JK}^{(v)}j(j+1)k^2-D_K^{(v)}k^4-(-1)^v\Delta/2, \quad (3)$$

where j is the total angular momentum, k is its projection on the symmetry axis, and v is the inversion quantum number. The rotational constants are found in Table I. In addition to the usual symmetric top energies (which depend on j and k), there will be a contribution from the inversion tunneling. The energy of symmetric inversion states ($v=0$) will be reduced by $\Delta/2$, while that for antisymmetric inversion states ($v=1$) will be increased by $\Delta/2$.

C. The basis functions

Each basis function will be a product of a radial function, an angular function, an inversion function, and an end-over-end ($e-o-e$) rotational function of the complex

$$\Psi = \psi(R)\psi(\theta,\phi)\psi(\rho)\psi(l). \quad (4)$$

The symmetry of the basis functions will be a direct product of the symmetry of the components. The radial functions, denoted $\chi_n(R)$, are obtained by contracting 50 distributed Gaussians on an effective radial potential. The eigenfunctions of the lowest six eigenvalues are then used as the radial basis. The form of the effective radial potential $V(R)$ used is that developed by Cohen.[1,35] The essential requirements of a model radial potential are that it is flexible enough to place the repulsive wall closer in than the closest region of the multidimensional IPS, and that its minimum is located near the global minimum of the IPS. It must be flexible enough to accommodate about 0.4 Å of change in the position of the repulsive wall and radial minimum as a function of θ and ϕ.

The radial potential developed by Cohen uses the same form as that employed in the IPS developed by Hutson,[28]

$$V(R) = A\ e^{\beta(R-R_{\rm ref})} - \sum_{n=6}^{8} C_n D_n(R) R^{-n}. \quad (5)$$

Here A, β, $R_{\rm ref}$, C_6, C_7, C_8 are parameters specified by the user to yield the best functions and points for the collocation routine. We found that $A=101.64$ cm^{-1}, $\beta=3.001$ Å^{-1}, $R_{\rm ref}=4.018$, $C_6=75.2\ E_h a_0^6$, $C_7=400\ E_h a_0^7$, and $C_8=10\,000\ E_h a_0^8$ leads to a potential that yields good collocation points and functions. The C_6 coefficient was fixed to its value for Ar–NH_3, and the C_7 and C_8 coefficients were fixed at the above values, while the other three parameters were determined by a least-squares fit of the lowest three vibrational energies along six different radial cuts through preliminary versions the full 3D surface when using the six contracted radial functions compared to the exact vibrational energies along those radial cuts. It is found that there is better performance when the model potential is somewhat deeper than the global minimum of the IPS; e.g., the rms difference between the exact vibrational energies and those obtained along the trial radial potential is 0.028 cm^{-1} when the trial potential is 265 cm^{-1} deep compared to 0.28 cm^{-1} when the trial potential is 160 cm^{-1} deep. We feel that bound state eigenfunctions make a better basis than unbound ones, and a deeper well results in more bound states. A final convenience of using a model radial potential is that the radial basis functions for the collocation calculation are orthogonal. This simplifies any integration of the final eigenvectors that may be desired in order to compute dipole moments or quadrupole coupling constants.

The angular basis is a symmetry-adapted product of two Wigner D matrices in the phase convention of Condon and Shortley:[5,36]

$$D^{J*}_{M\Omega}(\alpha,\beta,0) D^{j*}_{\Omega k}(\gamma,\theta,\phi), \quad (6)$$

where the first one describes the orientation of the vdW axis (R) in space, and the second one describes the orientation of the NH_3 in the body-fixed axis system.

The Ar–NH_3 complex is described by the permutation-inversion molecular symmetry group $D_{3h}(M)$,[37] which has six irreducible representations (Γ)—A_1', A_1'', A_2', A_2'', E', and E''. The character table for $D_{3h}(M)$ can be found in Table A9 of Ref. 37. The A_1' and A_1'' states have zero statistical weight for the isotopomer of NH_3 containing only hydrogens, and therefore we are free to omit the A_1' and A_1'' states from the calculation since there is not yet any data for the isotopically substituted complex. They are, of course, included when predicting Ar–ND_3 spectra. The symmetrization of the basis functions for the Ar–NH_3 complex is similar to that carried out for the Ar–H_2O complex,[1,5] but there are some important differences because Ar–NH_3 has doubly degenerate E' and E'' states that have no counterpart in Ar–H_2O.

TABLE II. Transformation properties of angular basis functions (see Ref. 21).

$PI(D_{3h})$	Effect on basis		
$\hat{E}$			$\lvert jk\Omega JM\rangle$
(123)		$\exp(2\pi ik/3)$	$\lvert jk\Omega JM\rangle$
(23)*	$(-1)^{J+k}$		$\lvert j-k-\Omega JM\rangle$
$\hat{E}$*	$(-1)^{J+j+k}$		$\lvert jk-\Omega JM\rangle$
(123)*	$(-1)^{J+j+k}$	$\exp(2\pi ik/3)$	$\lvert jk-\Omega JM\rangle$
(23)	$(-1)^{j}$		$\lvert j-k\Omega JM\rangle$

First, the wave functions of the noninverting Ar–NH_3 complex in its $J=0$ state are symmetrized; afterwards, the effects of inversion and $e-o-e$ rotation on the symmetry of the wave function can be easily added. The effect of each symmetry operation of the PI $D_{3h}(M)$ group on the angular basis shown in Eq. (6) has been given by van Bladel *et al.*,[21] and is reproduced in Table II. The basis functions given in Eq. (6) have been written in the Dirac notation $\lvert jk\Omega JM\rangle$.

Because only k and Ω change sign under these symmetry operations of the PI group, the state $\lvert jk\Omega JM\rangle$ can be specified by $\lvert k\Omega\rangle$. The symmetrized wave functions are

$$\lvert \pm\pm\rangle = 1/2[\lvert k\Omega\rangle + (-1)^{\xi}\lvert -k\Omega\rangle] + (-1)^{\epsilon}[\lvert k-\Omega\rangle + (-1)^{\xi}\lvert -k-\Omega\rangle](1+\delta_{0k})^{-1/2}(1+\delta_{0\Omega})^{-1/2}, \quad (7)$$

where ξ and ϵ can be 0 or 1. Thus, four different combinations arise:

$$\lvert ++\rangle = 1/2\ [(\lvert k\Omega\rangle + \lvert -k\Omega\rangle) + (\lvert k-\Omega\rangle + \lvert -k-\Omega\rangle)], \quad (7a)$$

$$\lvert -+\rangle = 1/2\ [(\lvert k\Omega\rangle - \lvert -k\Omega\rangle) + (\lvert k-\Omega\rangle - \lvert -k-\Omega\rangle)], \quad (7b)$$

$$\lvert +-\rangle = 1/2\ [(\lvert k\Omega\rangle + \lvert -k\Omega\rangle) - (\lvert k-\Omega\rangle + \lvert -k-\Omega\rangle)], \quad (7c)$$

$$\lvert --\rangle = 1/2\ [(\lvert k\Omega\rangle - \lvert -k\Omega\rangle) - (\lvert k-\Omega\rangle - \lvert -k-\Omega\rangle)]. \quad (7d)$$

Here both k and Ω are constrained to be positive, and the normalization factors of $(1+\delta_{0k})^{-1/2}$ and $(1+\delta_{0\Omega})^{-1/2}$ have been omitted for clarity. The first + or − in the angular basis function ket in Eqs. (7) refers to the symmetrization in k, or $(-1)^{\xi}$, while the second + or − refers to the symmetrization in Ω, or $(-1)^{\epsilon}$.

The effects of $e-o-e$ rotation and NH_3 subunit inversion can be included at this point, as discussed by Gwo.[38] The symmetry of the $e-o-e$ pseudodiatomic rotational

TABLE III. Symmetry of VRT states of Ar–NH_3 as a function of ϵ, ξ, J, j, k, and v.

$\epsilon+v+j+k+J$	$v+j+\xi$	k (mod 3)	Symmetry
even	even	0	A_1'
odd	even	0	A_1''
even	odd	0	A_2'
odd	odd	0	A_2''
even	···	≠0	E'
odd	···	≠0	E''

wave function is A_1' for even l rovibrational levels, and A_1'' for odd l rovibrational levels. Here l is the quantum number describing the $e-o-e$ rotation, where

$$l=\mathbf{J}-\mathbf{j}. \tag{8}$$

Therefore, the superscript of levels with odd l will have to be changed ($'\leftrightarrow''$) from that obtained for $J=0$. Similarly, Gwo determined the effects of inversion of the NH_3 subunit.[38] The results are that the symmetry of symmetric inversion states is A_1', and that for antisymmetric inversion states is A_2''. Again, the totally symmetric A_1' symmetry has no effect on the final symmetry, but the effects of A_2'' are a simultaneous change of both the sub and superscripts of the state given above, e.g., $A_1'\leftrightarrow A_2''$, $A_2'\leftrightarrow A_1''$, and $E'\leftrightarrow E''$. The symmetry of each basis state as a function of ϵ, ξ, J, j, k, and v in $J=0$ is given in Table III.

Until this point, the treatment has been analogous to that for Ar–H_2O,[1] but if the doubly degenerate E states are to be included in the calculation, we must choose one and only one of the two linear combinations of the two degenerate functions for each state. We originally tried performing the calculation including both degenerate functions (at the expense of a roughly eightfold increase in computational time), but this caused the collocation method to fail for unknown reasons. Therefore, it is imperative that the degenerate functions are correctly separated into two groups.

Equations (7a) and (7b) form one degenerate pair. States of E' symmetry are obtained from

$$1/\sqrt{2}(|++\rangle+(-1)^{\tau}|-+\rangle), \tag{9}$$

and states of E'' symmetry are obtained from

$$1/\sqrt{2}(|++\rangle-(-1)^{\tau}|-+\rangle), \tag{10}$$

where $\tau=0$ for k (mod 3)=1, and $\tau=1$ for k (mod 3)=2. Equivalently, Eqs. (7c) and (7d) form a degenerate pair which yield the following states of E' and E'' symmetry:

$$1/\sqrt{2}(|+-\rangle-(-1)^{\tau}|--\rangle), \tag{11}$$

$$1/\sqrt{2}(|+-\rangle+(-1)^{\tau}|--\rangle), \tag{12}$$

again letting $\tau=0$ for k (mod 3)=1, and $\tau=1$ for k (mod 3)=2.

The overall basis is a product of the radial basis and angular basis. The basis used for the *ortho* states of Ar–NH_3 is the same as used for Ar–H_2O:[1,5]

$$\Psi_{J,\Gamma}(\alpha,\beta,\gamma,R,\theta,\phi)$$
$$=\frac{1}{R}\sum_{\xi=0}^{1}\sum_{\epsilon=0}^{1}\sum_{\Omega=\epsilon}^{J}\sum_{j=\Omega}^{j_{\max}}\sum_{k=0}^{k_{\max}}\sum_{n=1}^{N_R}C_{\xi\epsilon\Omega jkn}\chi_n(R)$$
$$\times(1+\delta_{0\Omega})^{-1/2}\{D^{J*}_{M\Omega}(\alpha,\beta,0)S^{j\xi*}_{\Omega k}(\gamma,\theta,\phi)$$
$$+(-1)^{\epsilon}D^{J*}_{M-\Omega}(\alpha,\beta,0)S^{j\xi*}_{-\Omega k}(\gamma,\theta,\phi)\}, \tag{13}$$

where

$$S^{j\xi*}_{\Omega k}(\gamma,\theta,\phi)=(1+\delta_{0k})^{-1/2}\{D^{j*}_{\Omega k}(\gamma,\theta,\phi)$$
$$+(-1)^{\xi}D^{j*}_{\Omega -k}(\gamma,\theta,\phi)\}. \tag{14}$$

The basis for the *para* states is formed by taking the symmetric and antisymmetric combination of the appropriate symmetrized functions as discussed above.

The convergence of the basis has been rather difficult to quantify. The problem is twofold: (1) The convergence is not monotonic, and (2) there can be particularly bad bases for which the calculated energy levels change dramatically. That is, the energy calculated for a level converges toward a limiting value as a function of basis set used, but there can be certain bases that are particularly bad in comparison with other bases of similar size. We have found that bases with $k_{\max}=j_{\max}$ are to be avoided because there is a large amount of oscillation from the $e^{-ik\phi}$ term in the basis functions compared to the number of collocation points at which the functions are evaluated. Table IV presents some vibrational energy levels with $J=0$ as a function of basis set size. Rotational term values for states that are not strongly perturbed through the Coriolis interaction are determined to within 5 MHz for all the bases shown in Table IV, whereas states that are highly perturbed are determined to roughly 20 MHz.

The size of the basis used to derive the IPS is 6 contracted radial functions ($N_R=6$), 11 different values of j ($N_\theta=11$), i.e., $0\leqslant j\leqslant 10$ or $1\leqslant j\leqslant 11$, etc., and $k_{\max}=9$ for the A states ($N_\phi=4$), and $k_{\max}=8$ for the E states ($N_\phi=6$). The value of J ranges from 0 to 2, as does Ω. The total basis set size for the different symmetries vs J are given in Table V, but when the problem is solved, it is done so in blocks for each Ω and the results are then recoupled. Thus when $J>0$ the matrices that are actually diagonalized for each Ω subblock are about $(2J+1)/(2-\delta_{0\Omega})$ times smaller than the size of the basis shown in Table V.

D. The intermolecular potential energy surface

The goal of this work is to determine a detailed IPS for the Ar–NH_3 complex. In order to do this, the surface is parameterized and the entire collocation routine is executed inside a nonlinear least-squares loop in which the parameters describing the surface are adjusted until the difference between calculated and observed quantities are smaller than the uncertainty inherent in this model of the complex.

The form of the IPS will be that developed by Cohen *et al.*[1,5] and is based on the work of Le Roy *et al.*[39] and Hutson.[28] Long-range attractive forces of induction and dis-

TABLE IV. Convergence of the lowest few Σ vibrational levels with $J=0$. Part (a) displays convergence as a function of radial basis, where N_R is the number of radial functions included with $N_\theta=11$, $k^A_{\max}=6$, and $k^E_{\max}=10$. Part (b) displays convergence as a function of angular basis with N_R fixed at 6.

	Basis		$\Sigma(0_0, n=0)$	$\Sigma(1_0, n=0)$	$\Sigma(0_0, n=1)$	$\Sigma^a(1_1, n=0)$	$\Sigma^a(1_1, n=1)$	$\Sigma^s(2_1, n=0)$
(a)								
N_R								
9			−100.7121	−74.2341	−66.4905	−87.5579	−61.3055	−51.8811
8			−100.7126	−74.2341	−66.4900	−87.5584	−61.3049	−51.8809
7			−100.7125	−74.2344	−66.4904	−87.5581	−61.3046	−51.8808
6			−100.7110	−74.2328	−66.4885	−87.5564	−61.3020	−51.8787
5			−100.7127	−74.2338	−66.4842	−87.5579	−61.3013	−51.8784
(b)								
N_θ	$k^A_{\max}$	$k^E_{\max}$						
12	9	10	−100.6891	−74.2405	−66.4029	−87.5466	−61.2288	−51.8880
12	9	8	−100.6891	−74.2405	−66.4029	−87.5474	−61.2275	−51.8843
11	6	10	−100.7110	−74.2328	−66.4885	−87.5564	−61.3020	−51.8787
11	9	8	−100.6971	−74.2348	−66.4019	−87.5315	−61.2531	−51.8843
11	6	5	−100.7110	−74.2328	−66.4885	−87.5158	−61.2088	−51.9164
10	9	8	−100.7234	−74.1882	−66.4290	−87.6646	−62.1097	−51.8688

persion, and short-range coulombic and electron exchange repulsive forces constitute the IPS, specifically

$$V(R,\theta,\phi)=V^{\text{rep}}(R,\theta,\phi)+V^{\text{ind}}(R,\theta,\phi)+V^{\text{disp}}(R,\theta,\phi), \tag{15}$$

where

$$V^{\text{rep}}(R,\theta,\phi)=A(\theta,\phi)e^{-\beta(\theta,\phi)[R-R_{\text{ref}}(\theta,\phi)]}, \tag{16}$$

$$V^{\text{ind}}(R,\theta,\phi)=-\sum_{n=6}^{\infty} C_n^{\text{ind}}(\theta,\phi)R^{-n}, \tag{17}$$

$$V^{\text{disp}}(R,\theta,\phi)=-\sum_{n=6}^{\infty} C_n^{\text{disp}}(\theta,\phi)D_n(R)R^{-n}, \tag{18}$$

and the $D_n(R)$ are Tang–Toennies damping functions[28] that are needed to damp the dispersion at short range, where R^{-n} can get very large. The induction coefficients are not damped, because their contributions are small enough (see Table VII of Ref. 11) that a damping function would have negligible effect at the distances sampled by the surface. The quantities $A(\theta,\phi)$, $\beta(\theta,\phi)$, $R_{\text{ref}}(\theta,\phi)$, $C_n^{\text{ind}}(\theta,\phi)$, and $C_n^{\text{disp}}(\theta,\phi)$ are all quantities that are expanded in renormalized spherical harmonics.

Renormalized spherical harmonics $[Z_{lm}(\theta,\phi)]$ are used because the magnitude of their maxima and minima tend to not get much larger than unity, so the expansion coefficients will give a good measure of the amount of variation in the surface. The renormalized spherical harmonics are related to the usual normalized spherical harmonics, $Y_{lm}(\theta,\phi)$, by $Y_{lm}(\theta,\phi)=[(2l+1)/4\pi]^{1/2}Z_{lm}(\theta,\phi)$. The expansion in renormalized spherical harmonics of an arbitrary quantity $Q(\theta,\phi)$ is given by

$$Q(\theta,\phi)=\sum_{lm} Q_{lm}Z_{lm}(\theta,\phi), \tag{19}$$

where $Z_{lm}(\theta,\phi)$ are the renormalized spherical harmonics[40] which obey

$$Z_{l-m}=(-1)^m Z^*_{lm}. \tag{20}$$

The symmetry of NH_3 has two effects on the coefficients of this expansion. First, $Q_{lm}=0$ if m (mod 3)$\neq 0$ due to the threefold symmetry, second $Q_{l-m}=(-1)^m Q_{lm}$ because the xz plane is a plane of symmetry. Equation (19) can then be rewritten as

$$Q(\theta,\phi)=\sum_{0\leq m\leq l} Q_{lm}[Z_{lm}(\theta,\phi)+(-1)^m Z_{l-m}(\theta,\phi)] \times(1+\delta_{m0})^{-1}. \tag{21}$$

Combining Eqs. (20) and (21) yields

$$Q(\theta,\phi)=\sum_{0\leq m\leq l} Q_{lm}[Z_{lm}(\theta,\phi)+Z^*_{lm}(\theta,\phi)] \times(1+\delta_{m0})^{-1}, \tag{22}$$

and finally,[31]

$$Q(\theta,\phi)=\sum_{0\leq m\leq l} 2Q_{lm}(-1)^m\sqrt{\frac{(l-m)!}{(l+m)!}}P_{lm}(\cos\theta) \times\cos(m\phi)(1+\delta_{m0})^{-1}. \tag{23}$$

Equation (23) is the form of the expansion used throughout this work.

The unknowns of the potential shown in Eq. (15)—$A(\theta,\phi)$, $\beta(\theta,\phi)$, $R_{\text{ref}}(\theta,\phi)$, $C_n^{\text{ind}}(\theta,\phi)$, and $C_n^{\text{disp}}(\theta,\phi)$ are all expressed as expansions in renormalized spherical harmon-

TABLE V. Basis set size for different symmetries for different values of total angular momentum (J). $N_R=6$, $N_\theta=11$, $k_{\max}=9$.

J	A_2'	A_2''	E'	E''
0	144	156	270	270
1	462	474	810	810
2	⋯	810	1338	1338

ics, leading to 45 potential coefficients if the expansion for each quantity was taken out to the $Z_{53}(\theta,\phi)$ term. Rather than try to fit this many unknowns, especially since some of these will be highly correlated, we will parameterize the surface with the method developed by Le Roy *et al.*[39] and Hutson[28] and subsequently extended by Cohen,[1,5] and relate these parameters to the expansion coefficients described above.

The parameterization is identical to that used in Ref. 1. Briefly, the parameterization specifies the distance and depth of the radial minimum as a function of angles θ and ϕ, i.e., it specifies $R^m(\theta,\phi)$ and $\epsilon(\theta,\phi)$ where R^m is the position of the radial minimum and ϵ is the depth at the minimum, and these each are expansions in renormalized spherical harmonics. This parameterization is used for several reasons. First, it specifies the shape of the surface in the vicinity of the radial minimum, and the low lying bound states are localized within $\sim\pm 1$ Å of the radial minimum. Second, the inclusion of the low order induction and dispersion terms ensures the correct theoretical behavior at long range. Finally, anisotropy in the repulsive wall $\beta(\theta,\phi)$ and the preexponential factor $A(\theta,\phi)$ is included which allows the molecule to have some "shape." This parameterization has a very flexible functional form and does not suffer from high correlations between parameters, as long as unnecessary and/or undeterminable parameters are not included.

Table I lists constants and coefficients for NH_3 and Ar–NH_3 used in calculating $V(R,\theta,\phi)$. The dispersion coefficients are converted from the *ab initio* values reported by Wormer *et al.*[34] *Ab initio* values were used because the combination rules that approximate the dispersion coefficients require various molecular polarizabilities that are not well known from experiment. Wormer *et al.* used a slightly different coordinate system and basis for the expansion of the potential surface than we do, thus it was necessary to convert the coefficients obtained in that work to our coordinate system and spherical harmonic expansion.

Angular-radial coupling is an important effect of the IPS. In fact, the large amount of angular-radial coupling has prohibited the separation of angular and radial motions in the first place. One way that the angular-radial coupling will manifest itself is by splitting the free rotor states in $n=1$ by different amounts than in $n=0$, where n is the vdW stretching quantum number, and this is in fact observed for the *para* states.[15] It will also manifest itself by mixing $n=0$ with $n=1$ (and possibly more) wave functions. This was noted in our earlier treatment of Ar–NH_3 wherein an effective angular surface was determined and the quadrupole coupling constants were used as a measure of the angular-radial coupling.[11]

E. The collocation method

The collocation method is a very efficient way to solve the Schrödinger equation, $H\Psi=E\Psi$. Comprehensive descriptions of the collocation method as applied to atom-polyatomic systems can be found in Refs. 1 and 5, and only a brief description particular to this work is given here. Two techniques have been implemented to increase the speed of the calculation by a factor of 4 when $J=0$, and a factor of 28 when $J=2$, and they are discussed after the brief description of the collocation method.

One expresses Ψ as a linear combination of N basis functions:

$$\Psi=\sum_{j=1}^{N} c_j\phi_j(\mathbf{r}), \tag{24}$$

where $\mathbf{r}$ is a (configuration space) position vector. The collocation equations in this basis are given by

$$\sum_{j=1}^{N} (\langle \mathbf{r}_i|H-E|\phi_j\rangle)\mathbf{c}_j=0, \quad i=1,\ldots,N, \tag{25}$$

where the bracket notation signifies that the jth function is operated on by the Hamiltonian operator, and then evaluated at the ith point. These equations can be written as the generalized eigenvalue problem

$$\mathbf{Ax}=\lambda\mathbf{Bx}, \tag{26}$$

or in terms of Eq. (25),

$$\mathbf{Hc}_i=E_i\mathbf{Rc}_i, \tag{27}$$

where

$$\mathbf{H}_{ij}=\langle \mathbf{r}_i|H-E|\phi_j\rangle \quad \text{and} \quad \mathbf{R}_{ij}=\langle \mathbf{r}_i|\phi_j\rangle. \tag{28}$$

This form is reminiscent of the variational method, where one would use the more familiar matrix elements

$$\mathbf{H}_{ij}=\langle \phi_i|H-E|\phi_j\rangle \quad \text{and} \quad \mathbf{R}_{ij}=\langle \phi_i|\phi_j\rangle \tag{29}$$

instead. There are two consequences stemming from the differences in Eqs. (28) and (29). The most important one is that no integrals need be evaluated to calculate the matrix elements in Eq. (28); instead, the jth function is evaluated at the ith point to find $\mathbf{R}_{ij}$, while $\mathbf{H}_{ij}$ is obtained by operating on the jth function with the Hamiltonian and then evaluating it at the ith point. This is where the method derives its efficiency. The second, and less desirable consequence, is that the matrices $\mathbf{H}$ and $\mathbf{R}$ are not symmetric, thus the eigenvalues obtained are not guaranteed to be upper bounds of the true energy levels, and diagonalization of nonsymmetric matrices is less efficient than for symmetric matrices. Furthermore, the eigenvalues may be complex, and the eigenvectors are not guaranteed to be orthogonal to each other. We have found through experience that if enough points and functions are included in the basis to get reliable eigenvalues they will have negligible imaginary components, and the eigenvectors turn out to be very nearly orthogonal. In fact, the magnitude of the imaginary part of the complex eigenvalues are a valuable diagnostic for the adequacy of the basis set.

The number of points chosen must be the same as the number of functions in the basis if the equations are to be solved as the generalized eigenvalue problem. The number of functions in the basis is $N_R\times N_{\theta,\phi}$, where N_R is the number of radial functions and $N_{\theta,\phi}$ is the number of angular functions. Therefore, N_R radial points and $N_{\theta,\phi}$ angular points will be chosen. The radial points are chosen using the Harris, Engerholm, and Gwinn (HEG) method.[41]

Peet and Yang note that the HEG method provides the optimal points for calculating potential matrices by an N point quadrature,[27] and thus will be ideal for choosing the collocation points since the collocation method is equivalent to the variational procedure with all integrals approximated by an N point quadrature. The N_R radial points are taken to be the eigenvalues of the matrix whose elements are

$$R_{i,j}=\int \psi_i r \psi_j \, dr, \tag{30}$$

where r is the intermolecular center-of-mass separation. Thus, after the radial contraction has been performed, the eigenvectors of the lowest N_R eigenvalues are used to form the $N_R \times N_R$ HEG matrix, which in turn yields the collocation points in the radial coordinate upon diagonalization.

The determination of the points at which to evaluate the angular functions presents some difficulty for two reasons. First, there are two angular coordinates, θ and ϕ, but it is not a direct product basis in that each function in θ is not paired with each function in ϕ, i.e., they define a sphere, not a plane. Second, the Wigner D matrices are global, not localized, functions. For these two reasons we distribute the $N_{\theta,\phi}$ points as evenly as possible in the θ,ϕ coordinate space rather than trying to choose points that are each associated with a specific basis function.

Experience has shown that N_θ Gauss–Legendre points work well for the points in θ. These points are fairly uniformly spread in θ, but do not include $\theta=0°$ or $\theta=180°$. The majority of our effort when choosing points is spent in determining the optimum distribution of points in ϕ. Our current approach is to decide how many points are needed to sample the variation of the ϕ dependence of the basis functions and then cycle through these points as they are paired with the points in θ. The symmetry of the NH_3 monomer allows one to distribute the points on the interval $0 \leqslant \phi \leqslant \pi/3$ (instead of $0 \leqslant \phi \leqslant 2\pi$) since all values of ϕ can be mapped onto this interval through symmetry operations. Generally, one spaces the points in ϕ by $\pi/(k_{\max}+1)$ radians, which will yield one more point than the extrema of $\cos(k_{\max}\phi)$ or $\sin(k_{\max}\phi)$ on the region from 0 to π, thereby ensuring that the variation of the highest order function in ϕ will be adequately sampled. One uses $N_{\theta,\phi}/N_\theta$ points in ϕ for each point in θ, but they are not the same points in ϕ for each point in θ. For example, consider the A_2'' state in $J=0$ with $j_{\max}=6$ and $k_{\max}=6$. There will be 7 points in θ at the zeros of $P_7(\cos\theta)$ and 4 points in ϕ at 0, $\pi/4$, $\pi/2$, and $3\pi/4$, but there are only 15 angular functions of A_2'' symmetry, thus each point in θ cannot be paired with each point in ϕ. One would use two points in ϕ for each point in θ, with the extra point in ϕ used for $\theta=90°$, and the points would be chosen as follows: (θ_1,ϕ_1), (θ_1,ϕ_2), (θ_2,ϕ_3), (θ_2,ϕ_4), (θ_3,ϕ_1), (θ_3,ϕ_2), (θ_4,ϕ_3), (θ_4,ϕ_4), (θ_4,ϕ_1), (θ_5,ϕ_2), (θ_5,ϕ_3), (θ_6,ϕ_4), (θ_6,ϕ_1), (θ_7,ϕ_2), (θ_7,ϕ_3).

The spacing of the points in ϕ is determined by $k_{\max}+1$, but the wave functions have both $\sin(\phi)$ and $\cos(\phi)$ components. Thus, if the points are distributed on the extrema of $\cos(k_{\max}\phi)$ they will be on the nodes of $\sin(k_{\max}\phi)$. To avoid this, an offset of 1/4 the spacing is used when placing the points in ϕ, thereby ensuring that there will not be any functions that are sampled only at their nodes. These points chosen for the ϕ coordinate are Gauss–Chebychev points of order $k_{\max}+1$ that have been shifted.

The last two steps of the collocation method are exactly the same as in the Ar–H_2O case.[1,5] Briefly, we first operate on the wave function with the Hamiltonian, then integrate out the spatial dependence of the complex. These two steps are covered in detail in Refs. 1, 5, and 27. After performing these steps, one has a set of coupled differential equations in the three-dimensional coordinate space of the molecule (R,θ,ϕ).

Having chosen as many points as there are functions for a given total angular momentum J and symmetry representation Γ, the coupled differential equations are forced to be exact at the set of points, which casts the problem in the form of the generalized complex unsymmetrical eigenvalue problem:

$$[\mathbf{H}^{J,\Gamma}-E^{J,\Gamma}\boldsymbol{\Psi}^{J,\Gamma}]\mathbf{c}^{J,\Gamma}=0. \tag{31}$$

Finally, this generalized complex unsymmetrical eigenvalue problem is solved using standard packaged eigenanalysis routines (such as the NAG F02GJF or IMSL GVCRG) to yield eigenvalues and eigenvectors.

Two new features have been implemented to facilitate the calculation of the IPS. The first one is to avoid diagonalizing a matrix to calculate the derivatives of the Jacobian matrix when performing the least-squares fit by using the Hellman–Feynman theorem. The nonlinear least-squares loop requires the partial derivative of each residual with respect to each parameter in an effort to find the best solution to the problem. Originally, the generalized complex eigenvalue problem $\mathbf{Ax}=\lambda\mathbf{Bx}$ was solved to find the numerical derivative of each residual with respect to each parameter. Therefore, if there are n parameters, the generalized complex eigenvalue problem must be solved $n+1$ times for each step of the iteration. Since the eigenvectors of the diagonalization will change very little if the matrices $\mathbf{A}$ and $\mathbf{B}$ do not change much, the eigenvectors from the original diagonalization can be used to find the eigenvalues of the slightly perturbed situation rather than rediagonalizing the system. This is exactly the situation when the derivatives are being numerically determined for a given parameter by changing it by about one part in 10^5 and calculating the eigenvalues. The derivative of quantities such as the dipole moment or quadrupole coupling constants which are dependent on the wave functions must be obtained from a full diagonalization, however. Fortunately, these quantities are obtained from the A_2'' symmetry block with $J=0$ which is a relatively small matrix (see Table V), and only requires about 4 CPU seconds for diagonalization.

The generalized eigenvalue problem $\mathbf{Ax}=\lambda\mathbf{Bx}$ is first solved, and the eigenvectors $\mathbf{x}$ are saved and used to find the eigenvalues when one of the parameters of the IPS is adjusted by a small amount (one part in 10^5) when finding numerical derivatives. The new eigenvalues can be obtained by solving $\lambda=\mathbf{x}^{-1}\mathbf{B}^{-1}\mathbf{A}'\mathbf{x}$ where $\mathbf{A}'=\mathbf{A}_0+\mathbf{A}_1$, with $\mathbf{A}_0$ being the original matrix, and $\mathbf{A}_1$ being the small difference between the original and the one that needs to be solved to find

TABLE VI. Experimentally measured quantities of the *A ortho* states included in the fit. The uncertainties for the vibrational energies and rotational term value reflect the uncertainty of the model, but those for μ_a, eqQ_{aa}, and the second virial coefficients represent experimental uncertainties.

Vibrations:

Upper state	Lower state	$J' \leftarrow J''$	Symmetry	Freq. (MHz)	Unc. (MHz)	Obs.–Calc. (MHz)	Ref.
$\Pi(1_0, n=0)$	$\Sigma(0_0, n=0)$	1←0	$A_2' \leftarrow A_2''$	497 717.1	750.0	−169	11
$\Sigma(1_0, n=0)$	$\Sigma(0_0, n=0)$	1←0	$A_2' \leftarrow A_2''$	799 215.0	750.0	258	11
$\Sigma(0_0, n=1)$	$\Sigma(0_0, n=0)$	1←0	$A_2' \leftarrow A_2''$	1034 190.1	750.0	696	10
$\Delta(2_0, n=0)$	$\Sigma(0_0, n=0)$	2←0	$A_2'' \leftarrow A_2''$	1661 171.1	1000.0	−211	15

Term values:

State	$J' \leftarrow J''$	Symmetry	Freq.(MHz)	Unc.(MHz)	Obs.–Calc.(MHz)	Ref.
$\Sigma(0_0, n=0)$	1←0	$A_2' \leftarrow A_2''$	5753.3	5.0	2.3	10,11,14
$\Pi(1_0, n=0)$	1←1	$A_2'' \leftarrow A_2'$	177.4	5.0	−0.3	11
$\Pi(1_0, n=0)$	2←1	$A_2'' \leftarrow A_2'$	11 205.0	10.0	−1.7	11
$\Sigma(1_0, n=0)$	1←0	$A_2' \leftarrow A_2''$	5645.2	5.0	−6.5	10
$\Sigma(0_0, n=1)$	1←0	$A_2' \leftarrow A_2''$	5356.3	5.0	−5.7	11

Other:

State	Quantity	Value	Unc.	Obs.–Calc.	Ref.
$\Sigma(0_0, n=0)$	μ_a	−0.2803 D	0.007	0.003 D	14
$\Sigma(0_0, n=0)$	eqQ_{aa}	0.350 MHz	0.01	−0.010 MHz	14
$\Sigma(1_0, n=0)$	eqQ_{aa}	−0.84 MHz	0.10	0.07 MHz	11
$\Sigma(0_0, n=1)$	eqQ_{aa}	−0.19 MHz	0.15	−0.06 MHz	11
	2nd virial coeff. @ 296 K:	−43 cm^3/mol	6.0	−9.1 cm^3/mol	18
	2nd virial coeff. @ 273 K:	−52 cm^3/mol	9.0	−10.8 cm^3/mol	18
	2nd virial coeff. @ 253 K:	−62 cm^3/mol	10.0	−13.1 cm^3/mol	18
	2nd virial coeff. @ 238 K:	−73 cm^3/mol	15.0	−17.3 cm^3/mol	18

the numerical derivative. The "overlap" matrix **B** will not change because it is independent of the IPS. Thus,

$$\lambda = \mathbf{x}^{-1}\mathbf{B}^{-1}\mathbf{A}_0\mathbf{x} + \mathbf{x}^{-1}\mathbf{B}^{-1}\mathbf{A}_1\mathbf{x}, \tag{32}$$

but the first term is simply the eigenvalue already obtained when diagonalizing the unperturbed matrices, and only the change $\Delta\lambda$ need be found,

$$\Delta\lambda = \mathbf{x}^{-1}\mathbf{B}^{-1}\mathbf{A}_1\mathbf{x}. \tag{33}$$

Furthermore, since the kinetic energy and Coriolis terms in Eq. (1) are not affected by changing the IPS, we see that $\mathbf{A}_1 = \Delta V_{\text{diag}}\mathbf{B}$ where V_{diag} is a diagonal matrix where the ith element is the potential energy at the ith collocation point, and ΔV_{diag} is the change in V_{diag} after adjusting one of the parameters of the IPS by one part in 10^5. Equation (33) simplifies to

$$\Delta\lambda = \mathbf{x}^{-1}\mathbf{B}^{-1}\Delta V_{\text{diag}}\mathbf{B}\mathbf{x}. \tag{34}$$

It is found that the eigenvalues obtained in this fashion are good to about $\sim 10^{-6}$ cm^{-1} as compared to performing the full diagonalization on the perturbed system.

This is a very efficient way to find the numerical derivatives that are necessary for the nonlinear least-squares routine because in order to find them only the potential energy need be reevaluated at the collocation points. There is a small investment of time, however. One must invert and save **B** and **x**, and when performing the initial diagonalization, both eigenvalues and eigenvectors are required which necessitates slightly more CPU time. These two differences lead to approximately a factor of 3 more time than simply solving the generalized eigenvalue problem for **A** and **B**. The dividend of this investment is that it only takes about 1/10 as long to calculate each derivative required by the least-squares loop. Therefore, this method becomes more attractive as the number of parameters included in the fit is increased; it is 4 times faster when fitting 13 parameters. It takes roughly 4 CPU hours on an IBM RISC/6000 model 650 workstation to perform one full iteration of the least-squares loop with 13 parameters.

The generalized eigenvalue problem, and therefore the collocation method, do not require that **B** is invertible, whereas this method for speeding up the calculation most certainly does since **B** is explicitly inverted. It has been found however, that when reasonable answers (i.e., small imaginary components of the complex eigenvalues, and nearly orthogonal eigenvectors) are obtained from the collocation method, **B** is indeed invertible.

The second method employed to increase the speed was to exploit the fact that the potential is diagonal in $|\Omega|$, and only the Coriolis interaction will couple states of different $|\Omega|$. As discussed by van Bladel *et al.*[21] for a given J, final eigenvalues good to about 10^{-5} cm^{-1} are obtainable by diagonalizing each $|\Omega|$ subblock without including the off-diagonal Coriolis interaction, and then including the off-diagonal Coriolis matrix elements [Eq. (4) from Ref. 44] when recoupling the lowest 15 states from each Ω subblock. By solving the problem in this fashion the required computer

TABLE VII. Experimentally measured quantities of the *E para* states included in the fit. The uncertainties reflect the uncertainty of the model, not the experimental measurements.

Vibrations:

Upper state	Lower state	$J' \leftarrow J''$	Symmetry	Freq. (MHz)	Unc. (MHz)	Obs.–Calc. (MHz)	Ref.
$\Sigma_a(1_1, n=0)$	$\Sigma_s(1_1, n=0)$	1←1	$E' \leftarrow E''$	22 283.2	80.0	−224	12
$\Pi^{lower}(1_1, n=0)$	$\Sigma_s(1_1, n=0)$	1←0	$E'' \leftarrow E'$	51 765.0	200.0	−45	12
$\Pi^{upper}(1_1, n=0)$	$\Sigma_s(1_1, n=0)$	1←0	$E'' \leftarrow E'$	257 109.5	500.0	533	12
$\Pi^{upper}(2_1, n=0)$	$\Sigma^s(1_1, n=0)$	1←0	$E'' \leftarrow E'$	942 640.8	750.0	−479	15
$\Sigma^s(1_1, n=1)$	$\Sigma^s(1_1, n=0)$	1←0	$E'' \leftarrow E'$	1079 160.2	750.0	54	15
$\Sigma^a(1_1, n=1)$	$\Sigma^s(1_1, n=1)$	1←1	$E'' \leftarrow E'$	180 84.0	80.0	−81.3	15
$\Pi^{lower}(1_1, n=1)$	$\Sigma^s(1_1, n=0)$	1←0	$E'' \leftarrow E'$	1129 896.3	750.0	−1981	15
$\Delta^{lower}(2_1, n=0)$	$\Sigma_s(1_1, n=0)$	2←0	$E' \leftarrow E'$	1131 608.6	750.0	−679	15
$\Pi^{upper}(1_1, n=1)$	$\Sigma_s(1_1, n=0)$	1←0	$E'' \leftarrow E'$	1186 938.8	750.0	253	15
$\Delta^{upper}(2_1, n=0)$	$\Sigma^s(1_1, n=0)$	2←0	$E'' \leftarrow E'$	1363 563.6	750.0	1232	15
$\Pi^{lower}(2_1, n=0)$	$\Sigma^s(1_1, n=0)$	1←0	$E' \leftarrow E'$	1396 172.6	1000.0	−113	16
$\Sigma^s(2_1, n=0)$	$\Sigma^s(1_1, n=0)$	0←0	$E'' \leftarrow E'$	1506 652.9	1000.0	−1517	16
$\Sigma^a(2_1, n=0)$	$\Sigma^s(1_1, n=0)$	0←0	$E' \leftarrow E'$	1521 815.6	1000.0	−1085	16
$\Pi^{upper}(2_1, n=0)$	$\Sigma^s(1_1, n=0)$	1←0	$E' \leftarrow E'$	1541 934.8	1000.0	−378	16

Term values:

State	$J' \leftarrow J''$	Symmetry	Freq. (MHz)	Unc. (MHz)	Obs.–Calc. (MHz)	Ref.
$\Sigma_s(1_1, n=0)$	1←0	$E'' \leftarrow E'$	5033.98	5.0	−3.1	12
$\Sigma_s(1_1, n=0)$	2←1	$E' \leftarrow E''$	10 130.3	10.0	−6.3	12
$\Sigma_a(1_1, n=0)$	1←0	$E' \leftarrow E''$	4624.93	5.0	−3.2	12
$\Sigma_a(1_1, n=0)$	2←1	$E'' \leftarrow E'$	9509.0	10.0	3.1	12
$\Pi^{lower}(1_1, n=0)$	1←1	$E' \leftarrow E''$	375.63	10.0	−6.2	12
$\Pi^{lower}(1_1, n=0)$	2←1	$E' \leftarrow E''$	12 912.0	10.0	7.4	12
$\Pi^{lower}(1_1, n=0)$	2←2	$E'' \leftarrow E'$	930.0	20.0	−14.5	15
$\Pi^{upper}(1_1, n=0)$	1←1	$E' \leftarrow E''$	34.85	5.0	−0.5	15
$\Pi^{upper}(1_1, n=0)$	2←1	$E' \leftarrow E''$	11 417.0	10.0	3.5	15
$\Pi^{upper}(1_1, n=0)$	2←2	$E'' \leftarrow E'$	105.0	3.0	−1.3	15
$\Pi^{upper}(2_2, n=0)$	2←1	$E' \leftarrow E''$	10 639.0	10.0	2.5	15
$\Pi^{upper}(2_2, n=0)$	2←2	$E'' \leftarrow E'$	119.5	3.0	0.9	15
$\Delta^{lower}(2_1, n=0)$	2←2	$E' \leftarrow E''$	−0.8	2.0	−0.4	15
$\Sigma^s(1_1, n=1)$	2←1	$E' \leftarrow E''$	11 414.7	10.0	−9.9	15
$\Sigma^a(1_1, n=1)$	2←1	$E'' \leftarrow E'$	11 339.0	10.0	−3.9	15
$\Pi^{lower}(1_1, n=1)$	2←1	$E' \leftarrow E''$	10 936.5	10.0	−15.5	15
$\Pi^{lower}(1_1, n=1)$	2←2	$E' \leftarrow E''$	173.7	3.0	2.2	15
$\Pi^{upper}(1_1, n=1)$	2←1	$E' \leftarrow E''$	10 742.9	10.0	13.2	15
$\Pi^{upper}(1_1, n=1)$	1←1	$E' \leftarrow E''$	84.8	3.0	−1.9	15
$\Delta^{upper}(2_1, n=0)$	2←2	$E'' \leftarrow E'$	1.2	2.0	0.4	15
$\Sigma^s(2_1, n=0)$	1←0	$E' \leftarrow E''$	4117.8	5.0	−9.4	16
$\Sigma^s(2_1, n=0)$	2←1	$E'' \leftarrow E'$	8727.0	10.0	−13.2	16
$\Sigma^a(2_1, n=0)$	1←0	$E'' \leftarrow E'$	1447.6	5.0	8.1	16
$\Sigma^a(2_1, n=0)$	2←1	$E' \leftarrow E''$	6049.0	10.0	−27.1	16
$\Pi^{lower}(2_1, n=0)$	1←1	$E'' \leftarrow E'$	141.0	5.0	−1.4	16
$\Pi^{lower}(2_1, n=0)$	2←1	$E' \leftarrow E''$	10 727.8	10.0	−3.7	16
$\Pi^{lower}(2_1, n=0)$	2←2	$E' \leftarrow E''$	423.4	10.0	−2.4	16
$\Pi^{upper}(2_1, n=0)$	1←1	$E'' \leftarrow E'$	2506.0	5.0	−3.5	16
$\Pi^{upper}(2_1, n=0)$	2←1	$E' \leftarrow E''$	16 808.9	40.0	153.1	16
$\Pi^{upper}(2_1, n=0)$	2←2	$E' \leftarrow E''$	4853.3	10.0	35.2	16

time will scale roughly as $8J+1$ rather than $(2J+1)^3$. This results in a sevenfold increase in speed by $J=2$.

III. RESULTS

A. The data set

There have been roughly 95 FIR,[10,11] 91 submillimeter,[12] and 37 microwave[12,14] transitions previously assigned and published for Ar–NH_3, the accompanying paper reports 365 new FIR transitions, and Grushow *et al.*[16] have assigned 144 new transitions. Taken together, these transitions access 20 different VRT states which completely sample the angular coordinates of the complex, and sample from 3.4 to 4.4 Å in the radial coordinate. Dipole moments and quadrupole coupling constants have been measured for several states as well.[11,12,14] Second (interaction) virial coefficients for an Ar/NH_3 mixture at four different temperatures have recently been measured[18] and are included in the fit. Throughout this work, there has been ongoing interplay between assignment of the VRT data and refinements of the IPS. Previously pub-

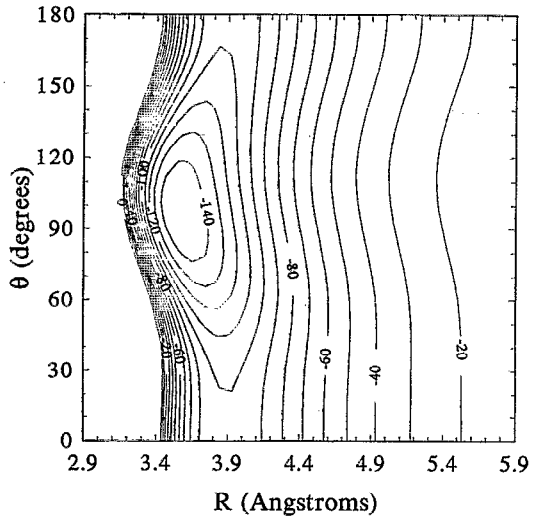

FIG. 2. Contour plot of Ar–NH_3 IPS at ϕ=60°. The 147 cm^{-1} deep global minimum of the surface is located at R=3.57 Å, θ=96.6°. Contours are separated by 10 cm^{-1}.

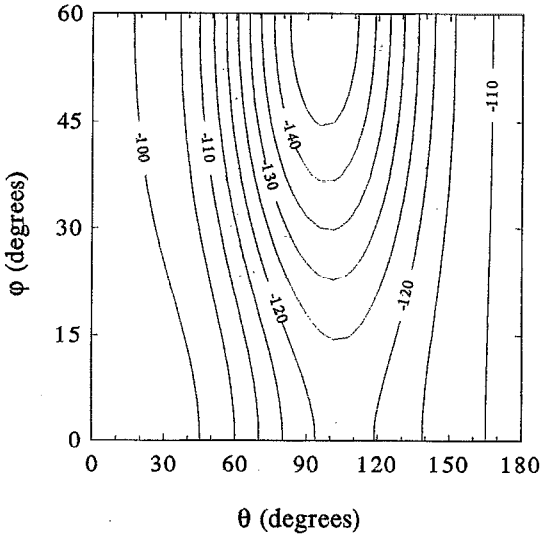

FIG. 4. Contour plot of $-\epsilon(\theta,\phi)$, the well depth at the radial minimum. Contours are separated by 5 cm^{-1}.

lished transition frequencies will not be reproduced here in the interest of saving space. These data can be found in Refs. 10–12, 14, 16, and in the accompanying paper. In the process of fitting the data, we use specific VRT energy levels and rotational term values, rather than the band origins and B values determined from a fit to a phenomenological model. This prevents any inadequacies of the phenomenological models used when fitting vibrational bands from affecting the IPS determination.

The quantities fit, and the agreement between observed and calculated values $(O-C)$ for these quantities are given in Tables VI and VII for the *ortho* and *para* states, respectively. The dimensionless root-mean-squared deviation (rmsd)[42] of the fit is 1.22 (where a value of 1 indicates that on average, all observations were fit to their stated uncertainty). The uncertainty assigned to each observation usually is an estimate of the accuracy of the model, but for μ_a, eqQ_{aa}, and the second virial coefficients it is the experimental uncertainty. The agreement with experiment is quite good. The largest discrepancies occur for the second virial coefficients and some of the rotational term values of the high lying *para* states, most of which are fit to within a factor of 2 of the estimated experimental uncertainty.

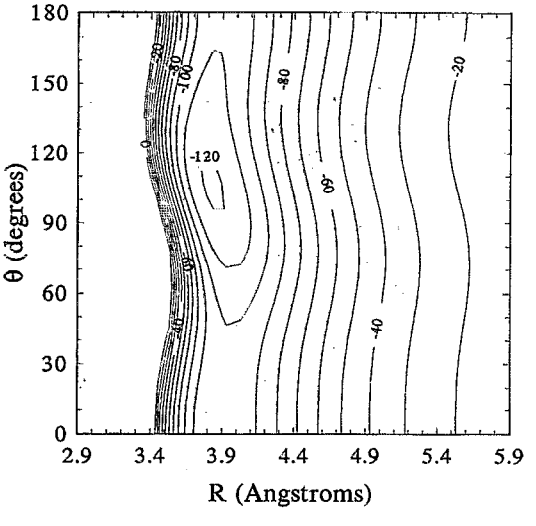

FIG. 3. Contour plot of Ar–NH_3 IPS at ϕ=0°. Contours are separated by 10 cm^{-1}.

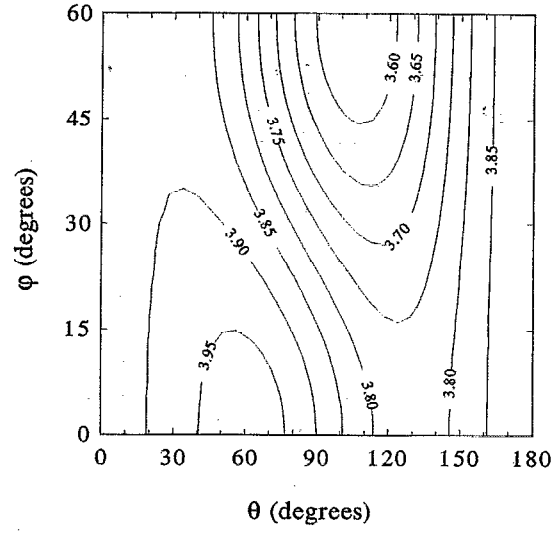

FIG. 5. Contour plot of $R^m(\theta,\phi)$, the position of the radial minimum. Contours are separated by 0.05 Å.

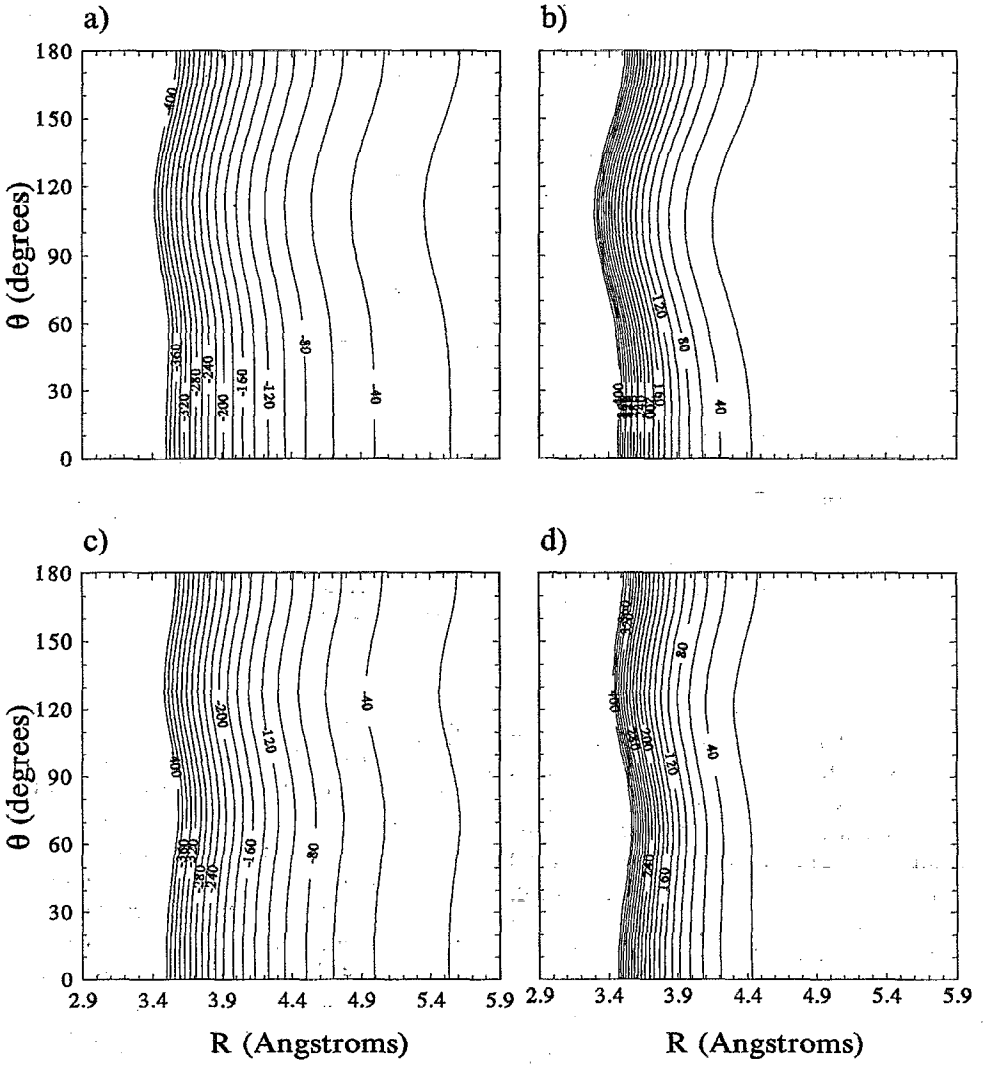

FIG. 6. Attractive and repulsive contributions to Ar–NH_3 IPS. Part (a) is attractive contribution at $\phi=60°$, part (b) is repulsive contribution at $\phi=60°$, part (c) is attractive contribution at $\phi=0°$, and part (d) is repulsive contribution at $\phi=0°$. Contours are separated by 20 cm^{-1}.

B. The intermolecular potential energy surface

The IPS determined from the fit is denoted AA1. The global minimum is 149.6 cm^{-1} deep and is found at $R=3.57$ Å, $\theta=96.6°$, and $\phi=60°$. This corresponds to a nearly T-shaped configuration with the Ar atom bisecting the angle between two hydrogens. When ϕ is fixed at 0°, the minimum shifts to $R=3.83$ Å, $\theta=105.6°$, and it is now 121.4 cm^{-1} deep. Thus, as the NH_3 is rotated from a position in which the Ar atom in is the half-plane containing the symmetry axis but is between two hydrogens to a position where the Ar is in the half-plane containing both the symmetry axis and a hydrogen, the minimum energy configuration is 28 cm^{-1} higher in energy than the global minimum, the center-of-mass separation increases by 0.26 Å, and θ increases from 96.6° to 105.6°, corresponding to the hydrogen end of NH_3 rotating away from the Ar. It must be emphasized that this is the position of the minimum on the surface, *not* the structure of the complex. In any VRT state, the complex is sampling a huge region of coordinate space, and does not have a well defined structure! Figures 2 and 3 show the potential energy as a function of two coordinates while holding the third one fixed. By choosing appropriate values for the fixed coordinate, one can ascertain the shape of the whole three-dimensional surface. The renormalized spherical harmonic expansions of $-\epsilon(\theta,\phi)$ and $R^m(\theta,\phi)$ are plotted as a function of θ and ϕ in Figs. 4 and 5, and Fig. 6 plots the attractive and repulsive terms separately as a function of R and θ.

Since the anisotropy of the Ar–NH_3 IPS is on the same order as the lowest rotational energy level spacings in free NH_3 (both on the order of 20 cm^{-1}), the NH_3 subunit undergoes nearly free internal rotation. Only the lowest A state energy level, $\Sigma(0_0, n=0)$, is not higher than all barriers to internal rotation. Although the wave function for any one state may be confined to certain regions of the surface, different states sample different regions, and thus the angular

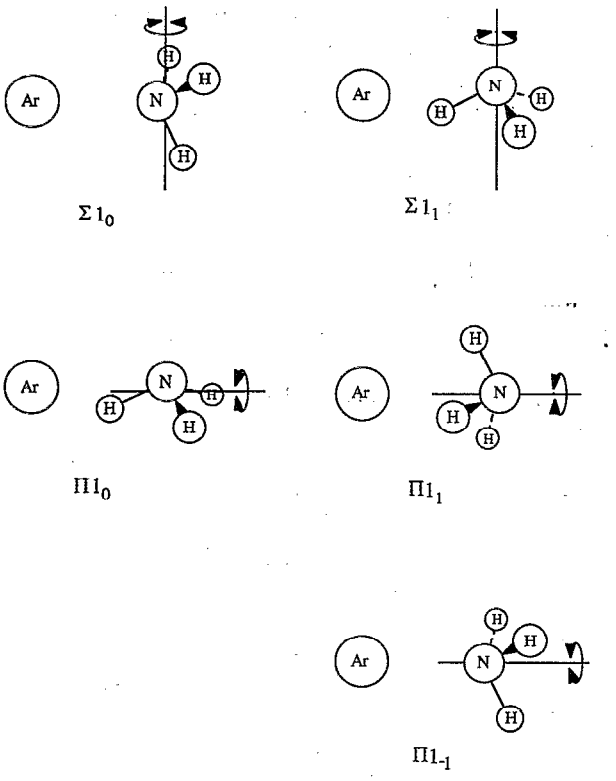

FIG. 7. Schematic representation of free internal rotations in $\Sigma(1_0, n=0)$, $\Pi(1_0, n=0)$, $\Sigma(1_1, n=0)$, and $\Pi(1_1, n=0)$ states.

coordinates of the surface are completely sampled by the states that we have measured.

The anisotropy in the potential splits energy levels that would otherwise be degenerate. Consider the $\Sigma(1_0, n=0)$ and $\Pi(1_0, n=0)$ states. The Π state samples the region near $\theta=90°$ while the Σ state samples the regions near $\theta=0°$ and 180° (see Fig. 7). Since the anisotropy in the surface causes the global minimum to occur near $\theta=90°$, the Π state is lower in energy. Figures 8(a) and 8(b) shows correlation diagrams for the vdW states with the free rotor NH_3 states.

Figures 2 and 3 are contour plots of $V(R,\theta,\phi)$ as a function of R and θ with ϕ held at 60° and 0°, respectively. An important observation is the following: while the global minimum of the IPS occurs at 3.57 Å, the center-of-mass separation obtained from the rotational constant of the $\Sigma(0_0, n=0)$ state is 3.83 Å.[11,14] This apparent contradiction arises from the fact that the $j_k=0_0$ free rotor wave function that is the primary contribution to the $\Sigma(0_0, n=0)$ ground state is isotropic in both the θ and ϕ coordinates. Thus, the repulsive wall encountered at $\phi=0°$ and at values of θ near 0° and 180° forces the $\Sigma(0_0, n=0)$ eigenstate to have a larger center-of-mass separation than found at the global minimum of the IPS. This discrepancy clearly demonstrates the importance of determining the full multidimensional IPS to extract structural information for vdW dimers rather than relying on spectroscopic constants determined only for a few states, as has been done for many WBCs.

Figure 3 clearly shows that one of the two dominant

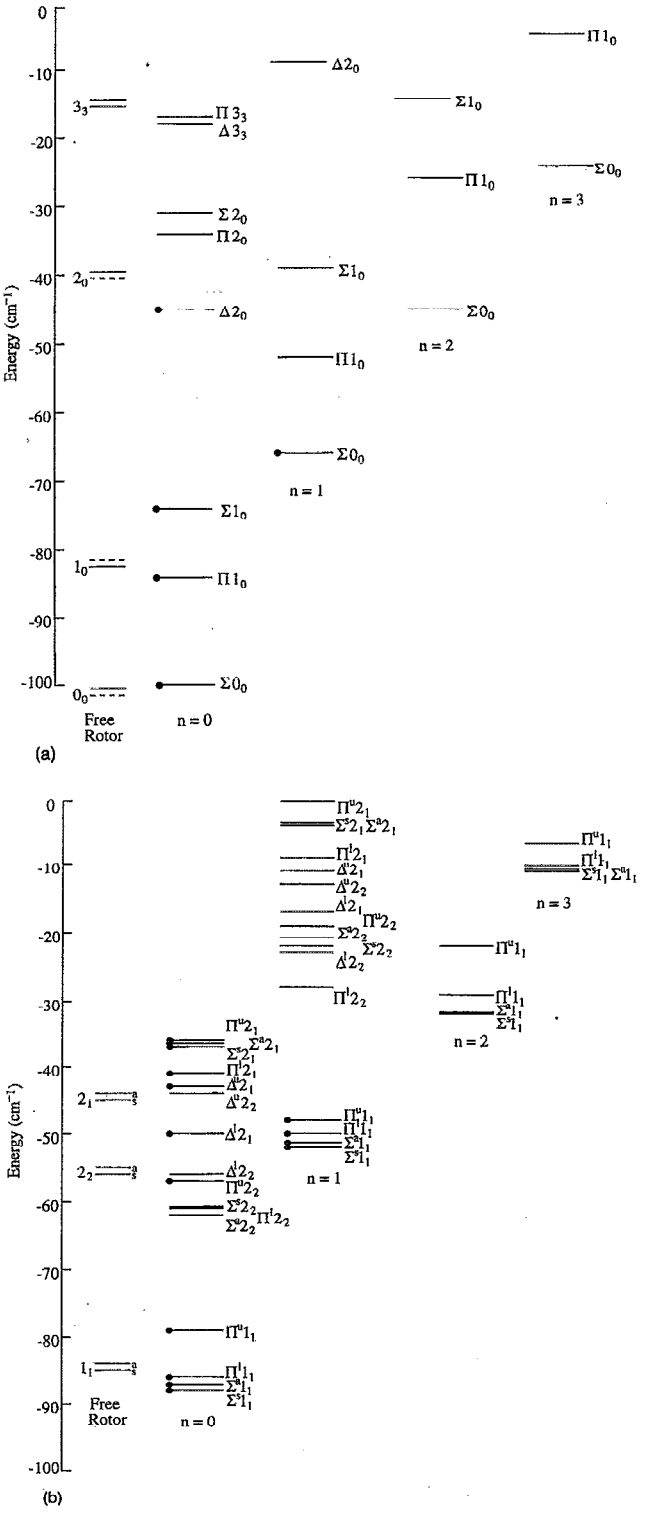

FIG. 8. Correlation of Ar–NH_3 vibrations to free rotor NH_3 states. Part (a) is for *ortho* states (A symmetry), part (b) is for *para* states (E symmetry). A solid circle placed on a VRT level indicates that it has been measured experimentally. For comparison, the free rotor levels have all been shifted down by 100.3 cm^{-1}, which is the energy obtained for the $\Sigma(0_0, n=0)$ state when the anisotropic terms of the IPS are neglected.

long-range attractions is directed along $\theta=60°$, $\phi=0°$, i.e., along the direction of the N–H bond. The other long-range attraction is directed along $\theta=180°$, and both are primarily due to the dispersion interaction. Even though the hydrogen

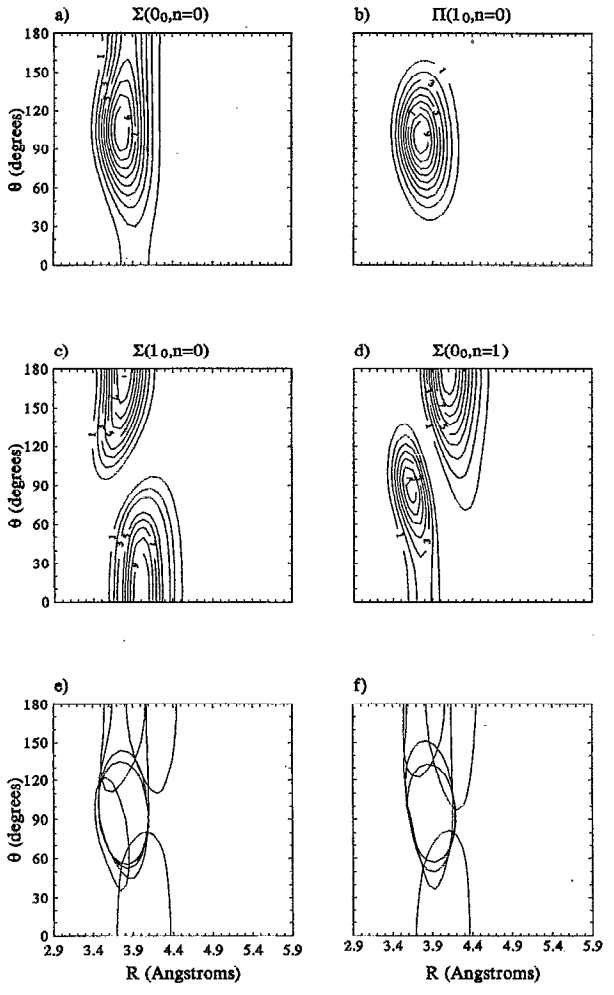

FIG. 9. Probability density for *ortho* states (A symmetry) as a function of R and θ with ϕ fixed at 60°. Each state is normalized to a maximum of 10. Part (a) is $\Sigma(0_0, n=0)$, part (b) is $\Pi(1_0, n=0)$, part (c) is $\Sigma(1_0, n=0)$, and part (d) is $\Sigma(0_0, n=1)$. Parts (e) and (f) are the probability densities at 30% of their maximum for the *ortho* states used to determine the IPS. The ϕ coordinate is fixed at 60° in part (e), and 0° in part (f).

bonded orientation is not the preferred orientation at the center-of-mass separations experienced by the complex, it is one of the preferred long-range orientations in accord with simple models.

Figure 4 plots $-\epsilon(\theta,\phi)$ vs θ and ϕ which represents the minimum energy path experienced by the Ar–NH_3 complex as a function of rotations in θ and ϕ. It is now possible to discuss the barriers to the internal motion without suffering from the effects of fixing the radial coordinate since $-\epsilon(\theta,\phi)$ is defined to be the energy at the radial minimum. There are two barriers to internal rotation in the θ coordinate; one is at 0° and the other at 180°. The lower of the two is through the $\theta=180°$ configuration where the value of R is 3.88 Å, and this barrier is 41 cm^{-1} above the global minimum. The barrier at $\theta=0°$ also occurs at $R=3.88$ Å and is 50 cm^{-1} above the global minimum. The barriers at $\theta=0°$ and $\theta=180°$ are independent of ϕ, as any quantity must be at these values of θ. The symmetry axis of the subunit is either parallel or antiparallel to the vdW axis at $\theta=0°$ and $\theta=180°$, thereby making it physically impossible for there to be any ϕ dependence of the IPS at these two values of θ. The barrier to rotation in the ϕ coordinate is 28 cm^{-1} above the global minimum, and it occurs at $\theta=105.6°$, $R=3.83$ Å (this is the minimum of the surface shown in Fig. 3 when ϕ is fixed at 0°). There is significant angular–angular coupling on this IPS in addition to the angular-radial coupling already discussed, viz. the position of the minimum of the IPS in one angular coordinate depends on the value of the other angular coordinate. As the NH_3 subunit rotates from $\phi=60°$ to $\phi=0°$, and the Ar atom moves from between two hydrogens to over a hydrogen, θ shifts from 96.6° to 105.6°, thereby rotating the hydrogen end of the molecule away from the Ar atom.

Figure 5 plots $R^m(\theta,\phi)$ as a function of ϕ and θ. From this figure it is possible to see how the center-of-mass separation of the Ar and the NH_3 change (for the minimum energy path) as a function of ϕ and θ. The qualitative features are similar to those in Fig. 4. This indicates that the orientations of lowest energy are also the orientations with the smallest intermolecular separation. The most prominent difference is a bulge in the region near $\theta=60°$. This configuration corresponds to the Ar being at nearly the same angle off the NH_3 symmetry axis as are the hydrogens (the hydrogens are at $\theta=69°$). Thus, it is not surprising that when θ is fixed at 60°, the center-of-mass distance is 0.20 Å larger at $\phi=0°$, where the Ar is along an N–H bond, compared to $\phi=60°$, where the Ar is between two hydrogens. Upon closer inspection, it is seen that the features in the $R^m(\theta,\phi)$ plot are shifted to larger values of θ compared to those in the plot of $-\epsilon(\theta,\phi)$, which means that the Ar and NH_3 can get closer together, but at a higher potential energy, when the hydrogens move out of the way.

The distance of closest approach of the radial minimum is seen to be 3.58 Å at $\theta=106.3°$, $\phi=60°$. This value of ϕ indicates that the Ar is in the half-plane that contains the NH_3 symmetry axis and is between two hydrogens, and $\theta=106.3°$ places the Ar in the gap between the lone pair of electrons of NH_3 and the repulsion of the hydrogens. Finally, it is evident how much angular-radial coupling is present in this complex when the NH_3 undergoes internal rotation. This is especially pronounced in the θ coordinate where center-of-mass distance at $\theta=106.3°$ is 0.33 Å smaller than at $\theta=180°$. In the ϕ coordinate the center-of-mass separation is 0.22 Å smaller at $(\theta,\phi)=(106.3°,60°)$ than at $(\theta,\phi)=(129°,0°)$, which is also a substantial variation in R^m as a function of angle.

Figures 6(a) and 6(b) present the attractive and repulsive contributions to the surface for $\phi=60°$, respectively. Figures 6(c) and 6(d) present these same contributions for $\phi=0°$. These depict the degree of repulsion and attraction that exists for $\phi=0°$, in the region near $\theta=69°$, i.e., along the direction of the N–H bond. It is also clear from (b) how much closer together the subunits can get when $\phi=60°$, especially at $\theta=110°$, which is the region of the "pocket" between the hydrogens and the lone pair of electrons. Naturally, the minimum occurs where the gradients due to attraction and repulsion are equal in magnitude and opposite in sign. Therefore, relatively small changes in either the attractive or repulsive

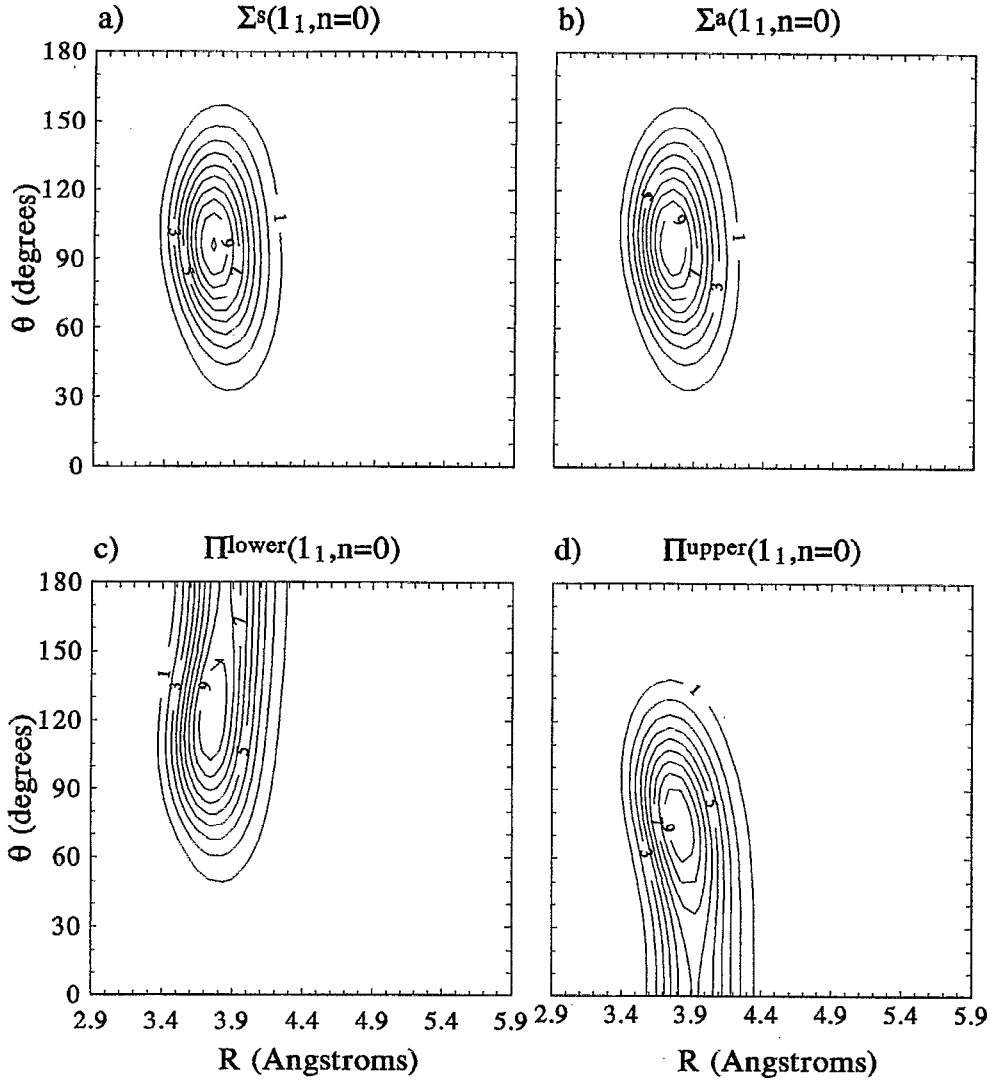

FIG. 10. Probability density for $\Sigma^s(1_1, n=0)$, $\Sigma^a(1_1, n=0)$, $\Pi^{lower}(1_1, n=0)$, and $\Pi^{upper}(1_1, n=0)$ as a function of R and θ with ϕ fixed at 60°.

contributions to the surface can shift the position of the minimum significantly. The maximum exchange repulsion will be in the regions of the hydrogens and the lone pair of electrons, but these same regions will also provide the maximum amount of attractive interaction due to dispersion. Thus, it is the intimate details of the balance of these two anisotropic interactions that shapes the experimentally determined surface. Finally, one notes that the exponentially decaying repulsive contribution to the surface falls off much more rapidly as a function of distance compared to the attractive contribution, implying that the long-range interactions are defined by the induction and dispersion coefficients.

C. VRT wave functions

Contour plots of the probability density $\Psi^*\Psi$ for the states included in the fit are plotted in Figs. 9 through 12. Each plot has been normalized to 10. The wave functions of the *ortho* states are plotted as a function of R and θ with ϕ fixed at 60° in Fig. 9. The high degree of angular-radial coupling between the $\Sigma(1_0, n=0)$ and $\Sigma(0_0, n=1)$ states is evident in (c) and (d) of Fig. 9. In the absence of angular-radial coupling, the wave function for the $\Sigma(1_0, n=0)$ state would not have any variation in R, much like that for the $\Sigma(0_0, n=0)$ ground state, and the wave function for the $\Sigma(0_0, n=1)$ state would not have any variation in θ, i.e., the nodal plane separating the regions of nonzero probability would be parallel to the R or θ axes. Part (b) of Fig. 9 clearly shows how the $\Pi(1_0, n=0)$ state samples the region near $\theta=90°$ making it the lowest energy state that correlates to $j_k=1_0$. Finally, parts (e) and (f) of Fig. 9 present the contours at 30% of the maximum probability for all five *ortho* states for $\phi=60°$ and $\phi=0°$, respectively. These give a good indication of the volume of coordinate space sampled by the *ortho* states that are included in the fit. The repulsion due to the hydrogen atoms is manifested in larger radial separations as seen in part (f) of Fig. 9 compared to part (e).

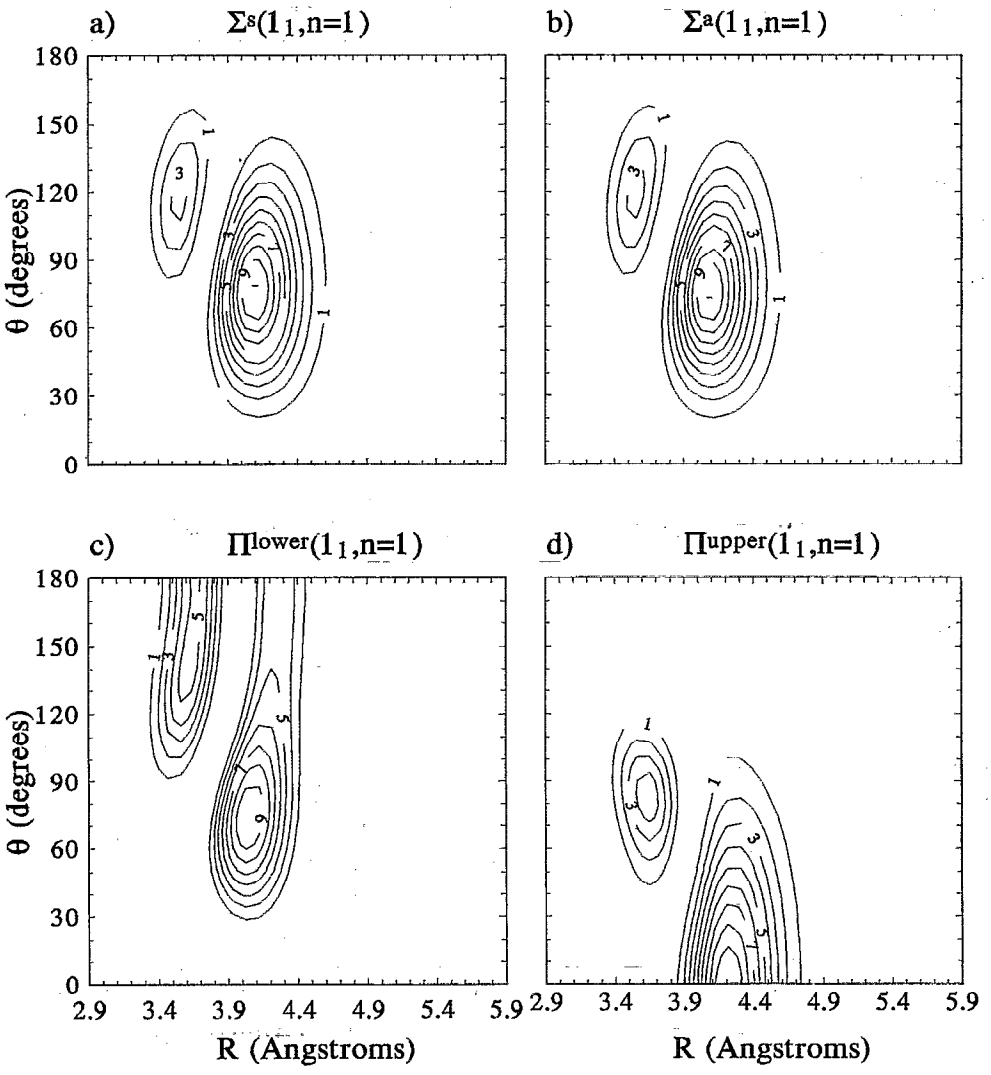

FIG. 11. Probability density for $\Sigma^s(1_1, n=1)$, $\Sigma^a(1_1, n=1)$, $\Pi^{lower}(1_1, n=1)$, and $\Pi^{upper}(1_1, n=1)$ as a function of R and θ with ϕ fixed at 60°.

Similar plots are presented for the *para* states in Figs. 10 through 13. The wave functions of the four states correlating with $j_k=1_1$ with $n=0$ are plotted in Fig. 10 for $\phi=60°$. Figure 11 plots the same four states with $n=1$. The Σ^s and Σ^a wave functions plotted with $n=0$ (Fig. 10) are seen to be nearly symmetric with respect to $\theta=90°$, which is why the inversion tunneling is practically unquenched in these states and they are separated by 22 GHz, compared to 24 GHz for free NH_3. Those for the Σ states with $n=1$ are not as symmetric with respect to $\theta=90°$, which explains why the inversion–tunneling splitting drops to 18 GHz in these states. The center-of-mass separation in the Σ states actually decreases in $n=1$ compared to $n=0$, which stems from the high degree of mixing with the $\Sigma(2_2, n=0)$ states. This initially surprising result is corroborated by the fact that the rotational constants of the Σ states with $n=1$ are larger than those in $n=0$.[15] Parts (c) and (d) of Figs. 10 and 11 plot the wave functions for the $\Pi 1_1$ states with $n=0$ and $n=1$. It is clear that one Π state mainly samples the region near $\theta=0°$, while the other mainly samples the region near $\theta=180°$. The $\Pi^{upper}(1_1, n=1)$ state is also seen to exhibit a high degree of angular-radial coupling.

The wave functions of the states correlating to $j_k=2_1$ are plotted in Fig. 12 for $\phi=60°$. The inversion–tunneling splitting of the $\Sigma 2_1$ states is measured to be about 14 GHz,[16] which explains why these states are not as symmetric with respect to $\theta=90°$ as the other Σ states are. It is also clear from this figure that the $\Delta 2_1$ states sample the deepest part of the potential, which makes them have the lowest energy of the states correlating to $j_k=2_1$. Similarly, it is seen that the lower energy $\Pi 2_1$ state primarily samples a region near $\theta=180°$, with a secondary maximum at 70°, while the higher energy $\Pi 2_1$ state mainly samples the region near $\theta=0°$. The $\Sigma 2_1$ states mainly sample the region near $\theta=50°$, and have a secondary maximum near 140°.

Finally, the contours at 30% of the maximum for all the

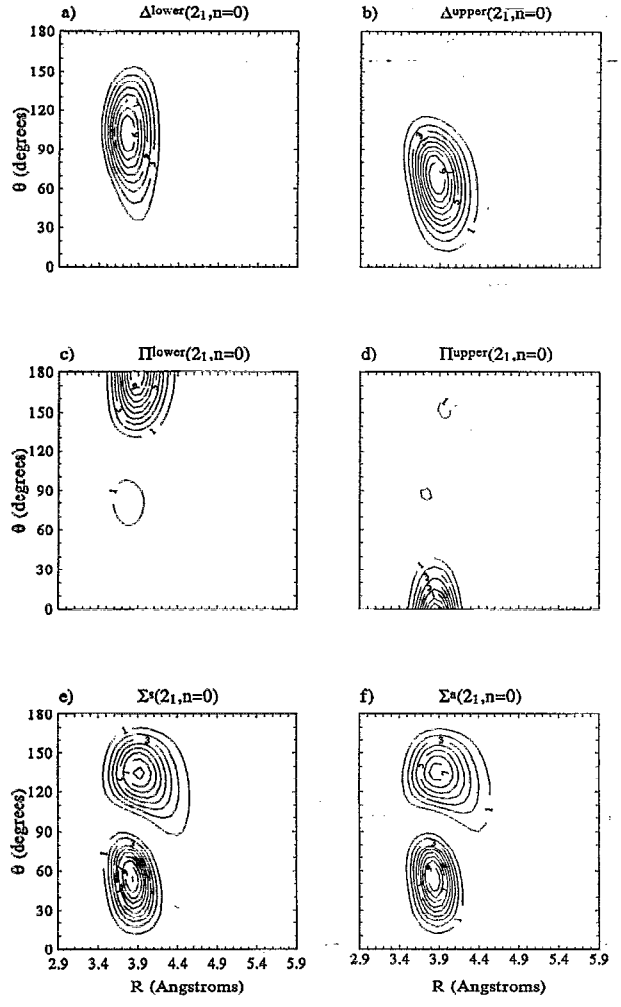

FIG. 12. Probability density for $\Delta^{\text{lower}}(2_1, n=0)$, $\Delta^{\text{upper}}(2_1, n=0)$, $\Pi^{\text{lower}}(2_1, n=0)$, $\Pi^{\text{upper}}(2_1, n=0)$, $\Sigma^{s}(2_1, n=0)$, and $\Sigma^{a}(2_1, n=0)$ as a function of R and θ with ϕ fixed at 60°.

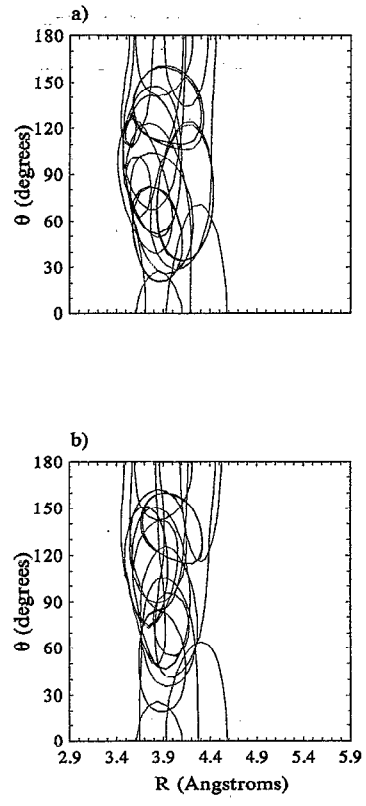

FIG. 13. Contour at 30% of the maximum of the probability densities for the *para* states used to determine the IPS. Part (a) is at ϕ=60°, part (b) is 0°.

para states included in the fit are plotted for ϕ=60° and 0° in Fig. 13 parts (a) and (b), respectively. It is seen that a slightly larger radial region is sampled by the *para* states compared to the *ortho* states. This arises for two reasons, the first is that the *para* states studied here are in general higher in energy than the *ortho* states (see Fig. 8), and this gives them a larger classically accessible region. Even the lowest energy *para* states are about 12 cm^{-1} above the lowest *ortho* state. The second reason is that the high density of states leads to a large degree of mixing, so even the states that are labeled $n=0$ can have significant $n=1$ character, except for the states correlating to $j_k=1_1$ with $n=0$.

D. The experimentally determined parameters

Table VIII presents the parameters and uncertainties, as obtained from the fit. Care was taken in the final fit to ensure that each parameter was well determined, i.e., that the magnitude of a parameter is greater than its uncertainty. In order to achieve this, some parameters must remain fixed during the nonlinear least-squares routine. Fixed parameters were held at zero in the absence of a good reason to fix them at anything else.

The correlations between parameters were quite small; the magnitude of the correlation between all pairs of parameters except two was less than 0.91. The largest correlation is between ϵ_{00} and β_{00} and is -0.97. These two parameters are often highly correlated in this type of fit since the spectroscopic data determines the shape of the well far more precisely than the well depth, and simultaneous change in these two parameters can essentially raise or lower the whole well without appreciably changing its shape. These parameters are not as highly correlated as they might have been since the virial coefficient data were included, thereby giving an independent measure of the well depth. The second largest correlation is between β_{20} and ϵ_{20}, and is 0.91. A noteworthy point is that the largest correlation between ϵ_{20}, R_{20}^{m}, or β_{20} with ϵ_{33} or R_{33}^{m} is only -0.63, and that these two sets of parameters contribute about the same amount to the surface. Van Bladel *et al.*[21] have suggested that at $R \approx 3.75$ Å the contribution from the V_{33} terms is about 15 times larger than that from V_{20} terms on the basis of the agreement of predictions from the *ab initio* surface of Bulski *et al.*[20] with experimental data. The effective angular surfaces determined from experimental data[11,12] were unable to determine the V_{33} contribution because the data measured were insensitive to this aspect of the surface. By including the recently measured Berkeley data and simultaneously fitting almost all other

TABLE VIII. Results of fit: Parameters with 1σ uncertainties, RMSD of fit, and correlations.

Parameter	Value	Uncertainty	Units
ϵ_{00}	120.85	0.82	cm^{-1}
ϵ_{10}	−9.967	0.04	cm^{-1}
ϵ_{20}	−21.767	0.23	cm^{-1}
ϵ_{30}	5.353	0.09	cm^{-1}
ϵ_{33}	13.239	0.16	cm^{-1}
ϵ_{40}	5.410	0.15	cm^{-1}
R^m_{00}	3.793 45	0.0012	Å
R^m_{10}	0.101 98	0.0009	Å
R^m_{20}	0.091 02	0.0015	Å
R^m_{30}	−0.102 11	0.0025	Å
R^m_{33}	−0.135 96	0.0014	Å
β_{00}	3.4360	0.036	$Å^{-1}$
β_{20}	−0.3072	0.054	$Å^{-1}$

RMSD of fit=1.22

Correlation matrix:

β_{00}	1.00												
ϵ_{00}	−0.97	1.00											
ϵ_{10}	−0.45	0.46	1.00										
ϵ_{20}	0.39	−0.38	−0.18	1.00									
ϵ_{30}	−0.10	0.14	0.22	−0.58	1.00								
ϵ_{33}	−0.46	0.49	0.13	−0.70	0.45	1.00							
ϵ_{40}	0.49	−0.48	−0.12	0.43	−0.30	−0.60	1.00						
R^m_{00}	−0.83	0.80	0.44	−0.19	0.03	0.22	−0.26	1.00					
R^m_{10}	0.01	−0.17	0.23	0.34	−0.08	−0.30	0.05	0.02	1.00				
R^m_{20}	−0.15	0.27	0.21	−0.45	0.61	0.27	0.11	0.13	−0.56	1.00			
R^m_{30}	0.37	−0.51	0.05	0.48	−0.25	−0.41	0.34	−0.25	0.84	−0.67	1.00		
R^m_{33}	−0.17	0.03	−0.04	0.33	−0.27	−0.13	−0.31	0.12	0.73	−0.66	0.58	1.00	
β_{20}	0.31	−0.35	−0.32	0.91	−0.56	−0.47	0.18	−0.19	0.49	−0.67	−0.58	0.60	1.00
	β_{00}	ϵ_{00}	ϵ_{10}	ϵ_{20}	ϵ_{30}	ϵ_{33}	ϵ_{40}	R^m_{00}	R^m_{10}	R^m_{20}	R^m_{30}	R^m_{33}	β_{20}

available data, the contributions from V_{20} and V_{33} terms have finally been separated, and the results are *not* in agreement with the *ab initio* predictions.

The most direct method for verifying the contribution of V_{33} terms to the IPS would be to measure transitions to Ar–NH_3 states correlating with $j_k=3_3$ because the $\Sigma(3_3, n=0)$ states will be the first ones to directly sample the threefold variation of the IPS as a function of ϕ. There are two Ar–NH_3 states that correlate to $j_k=3_3$, one is of A_2'' symmetry, and the other A_2' symmetry. The former state can interact with the A_2'' ground state (which correlates to $j_k=0_0$) through the ϵ_{33} term of the IPS, but the one of A_2' symmetry cannot, and this results in a large energy separation. The $\Sigma 3_3$ A_2' state is predicted to be 82.3 cm^{-1} above the ground state, and the $\Sigma 3_3$ A_2'' state is predicted to be 88.8 cm^{-1} above the ground state due to the above mentioned interaction. The correlations among the V_{33} and V_{20} terms can then be eliminated by experimentally determining the energy of the A_2' and A_2'' states of Ar–NH_3 that correlate to $j_k=3_3$. Unfortunately, the transition dipole from the ground state to states correlating to $j_k=3_3$ are very small which makes it difficult to measure a direct transition. The transition moment calculated for the most intense of these transitions is about 0.012 D, compared to 0.19 D for the $\Sigma(0_0, n=1)\leftarrow\Sigma(0_0, n=0)$ transition. Fortunately, the V_{33} contribution to the IPS is also manifested in interactions between states with $k=1$ and those with $k=2$. Since these states occur in pairs, the effects of the V_{33} terms in the IPS are not as transparent as in the example above with $j_k=3_3$, but their contribution can indeed be determined given enough experimental data. In fact, measurements of the $j_k=1_1$, $j_k=2_2$, and $j_k=2_1$ states have allowed both us and Grushow *et al.*[16] to determine the V_{33} contribution to the surface.

Further tests to verify the accuracy of the IPS include measurement of the spectrum of the perdeuterated complex, Ar–ND_3, and to measure transitions to states of higher energy in Ar–NH_3. The $\Sigma(1_0, n=1)$, $\Sigma^s(1_1, n=2)/\Sigma^s(2_2, n=1)$, and $\Pi^{\text{lower}}(2_2, n=2)/\Pi^{\text{lower}}(1_1, n=2)$ states are good candidates because they have reasonably strong transition dipoles from the ground state (about 0.19 D), and they are within 30 to 40 cm^{-1} of dissociation. The accuracy of repulsive regions of the surface will be best tested by comparing rotational excitation cross sections of NH_3 by collisions with Ar with those calculated from this IPS (see Sec. IV B).

There are only two contributions to $\beta(\theta,\phi)$—β_{00} and β_{20}. The value of $\beta(\theta,\phi)$ gives the steepness of the repulsive wall at a particular value of (θ,ϕ), where a large value for $\beta(\theta,\phi)$ implies a very steep repulsive wall [see Eq. (16)]. The isotropic value is 3.482 $Å^{-1}$. The β_{20} term is -0.353 $Å^{-1}$, which causes the repulsive wall to become steeper at $\theta=90°$, and less steep at $\theta=0°$ and $\theta=180°$. There are two issues

involving the repulsive terms that must be addressed. One is that there is not a β_{10} parameter, but there is a fairly sizable β_{20} parameter which brings into question whether or not the expansion in spherical harmonics has been carried out far enough. The second issue is that there are not β_{30} and β_{33} terms to provide steric repulsion from the hydrogen atoms directly. Both of these issues can be addressed as follows: Many fits were attempted with a wide variety of terms for the expansion of $\beta(\theta,\phi)$, and satisfactory results were obtained only when the β_{00} and β_{20} terms were the only ones included. More importantly, it is seen from Figs. 2 through 6 that there is indeed variation in the repulsive wall of the IPS in the vicinity of the hydrogen atoms. This variation arises even when β_{30} and β_{33} terms are not explicitly included because the surface is a combination of attractive and repulsive contributions, and variation in the attractive contribution (the ϵ_{30}, ϵ_{33}, R^m_{30}, and R^m_{33} terms are all significant) can affect the effective behavior of the repulsion. The coupling of the attractive and repulsive contributions to the surface is also explicit because $R_{\rm ref}(\theta,\phi)$ in Eq. (16) is set equal to $R^m(\theta,\phi)$ during the parameterization of the IPS in order to reduce the number of unknown parameters.

Finally, if $(\pi-\theta)$ were substituted for θ in IPS, the vibrational energies and rotational term values would not change. The only changes would be the sign of quantities that are projections of the odd multipole moments of the NH_3 monomer on the vdW axis, i.e., the dipole moment, octopole moment, etc. The significance of this observation lies in the fact that the magnitude, but not the sign, of the dipole moment of Ar–NH_3 has been determined experimentally.[14] Upon initial consideration, it would seem that there would be an ambiguity in the sign of the β_{lm}, ϵ_{lm}, and R^m_{lm} parameters when $(l+m)$ is odd, i.e., that it would be possible to simultaneously change the sign of all these parameters without affecting the eigenvalues and wave functions determined from the IPS. This does not occur, however, because the signs of the low order dispersion and induction coefficients *are* known, and these coefficients remain fixed during a fit. We attempted to fit the experimentally measured quantities to an IPS wherein the sign of all parameters with odd $(l+m)$ had been changed. While the rmsd of the fit did not get significantly larger, the shape of the surface became unphysical. That is, the regions of closest approach were directly along the N–H bond, and the long-range behavior was in disagreement with that expected from the theoretically determined induction and dispersion contributions. The high order induction and dispersion coefficients were much too large and offset the contribution from the low order coefficients that are known from theory. Attempts were also made to fit the data when changing the sign of some, but not all, of the coefficients with odd $(l+m)$, and the eigenvalues obtained were completely unreasonable. We thus conclude that the sign of the ground state dipole moment of Ar–NH_3 is negative. That is, that the vibrationally averaged projection of the permanent NH_3 dipole moment points away from the Ar atom. In other words, the expectation value of $\cos\theta$ is negative in the ground state.

IV. DISCUSSION

A. Internal motions: Hindered rotations and NH_3 inversion

It is the hindered rotations of the monomer due to the anisotropy in the IPS that give rise to the bending vibrations of the complex and the rich variety of spectroscopic features. A qualitative understanding of the ordering of the lowest few Ar–NH_3 bending vibrational levels is attained by considering the regions of the potential that are sampled by the free rotor wave functions that a particular state most nearly correlates with.

If the motion for the NH_3 subunit shown in Fig. 7 is compared with the IPS shown in Figs. 2–4, it is appreciated that the $\Pi(1_0, n=0)$ state samples, on average, regions with lower energy than the $\Sigma(1_0, n=0)$ state. This will lead to a lowering of the energy for the $\Pi(1_0, n=0)$ state relative to the $\Sigma(1_0, n=0)$ and is a sensitive measure of the ϵ_{20} term of the surface. Had there been a minimum on the IPS at $\theta=0°$ and possibly a secondary minimum at $\theta=180°$, then the ordering of these two levels would be reversed, such as is the case in Ar–HCl.[4] The ordering and separation of the $\Sigma(1_0, n=0)$ and $\Pi(1_0, n=0)$ in Ar–NH_3 unambiguously determines the contribution of the ϵ_{20} coefficient.

Similar arguments hold for the order and separation of the $\Delta(2_0, n=0)$, $\Pi(2_0, n=0)$, and $\Sigma(2_0, n=0)$ states. The θ dependence for these functions, in the limit of free internal rotation, is $\sin^2\theta$, $\sin\theta\cos\theta$, and $3\cos^2\theta-1$, respectively.[31] Thus, it is seen that the θ dependence of ψ^2 will be in the region of 90° for the $\Delta(2_0, n=0)$ state, and will be localized further from 90° in going to the $\Pi(2_0, n=0)$ state, and will be even further away from $\theta=90°$ in the $\Sigma(2_0, n=0)$ state. Thus, the Δ state is expected to be lowest in energy, followed by the Π state, and finally the Σ state.

The θ dependence of the functions that correlate to free rotor states of NH_3 that have $k=0$ is always symmetric (or antisymmetric) with respect to $\theta=90°$. Since the internal rotations are fast compared to the inversion–tunneling frequency ($0.8\ \text{cm}^{-1}$), the inversion coordinate effectively samples a symmetric environment. It would therefore be expected that the inversional motion is not quenched in the lowest few states with $k=0$ where the density of states is low. An alternative way to realize the absence of quenching in these states is that the basis state is freely inverting, and the only way to quench this inversion will be through mixing with basis states of opposite inversion symmetry, i.e., the only way for the inversion to be quenched in the $\Sigma(0_0, n=0)$ state is if the potential mixes in some $\Sigma(1_0, n=0)$ character, and those states have sufficiently different energies that there is very little mixing (see Table XI). Since one of the inversion levels of every pair is forbidden for the $k=0$ states of NH_3, it is impossible to measure the inversion–tunneling splitting directly in these states. The nuclear spin weights of the perdeuterated form of ammonia, ND_3, do allow both inversion symmetries for each inversion pair. Measurement of the FIR spectrum of Ar–ND_3 would reveal the amount of inversion in the ND_3 subunit in the states that correlate with $k=0$ free rotor states (the A states). The gas phase ND_3 inversion frequency is 1600 MHz,[33] and is thus easily resolv-

able. The ND_3 subunit would be more hindered than NH_3 by the IPS as well, which would make this an ideal candidate to probe the asymmetry of the environment of the inversion coordinate. Table IX lists the predicted energy levels for Ar–ND_3 obtained from the AA1 IPS.

The E states of Ar–NH_3 behave quite differently than the A states discussed above. For example, an Ar–NH_3 state that correlates with $j_1=1_1$ with $\Omega=1$ can sample either the region near $\theta=0°$ or $\theta=180°$, which leads to a splitting of the parity doublets that comprise that state since the potential has lower energy in the region near 180° than in the region near $\theta=0°$. This also leads to the quenching of the inversion of the NH_3 subunit since there is now an asymmetry along the inversion coordinate. Similarly, states of Ar–NH_3 with $\Omega>0$ that correlate with the $j_k=2_1$ and $j_k=2_2$ states of NH_3 will have the NH_3 inversion quenched. Namely, eigenfunctions of Ar–NH_3 that are comprised of roughly symmetric or antisymmetric combinations of the basis states will have a θ dependence that is *not* symmetric (or antisymmetric) about $\theta=90°$. This is because the basis states are made up of symmetric and antisymmetric combinations of states in which the θ dependence is not symmetric or antisymmetric about $\theta=90°$. Therefore, the probability of finding the eigenstate at a certain value of θ (or $180°-\theta$) will not be symmetric with respect to $\theta=90°$, and the inversion coordinate of the NH_3 subunit will have an asymmetric environment thereby quenching the inversion tunneling of the NH_3 subunit. It has been found experimentally that the inversion of the NH_3 subunit in the $\Sigma_s(1_1, n=0)$ and $\Sigma_a(1_1, n=0)$ states is undergoing nearly free inversion, and that it is almost completely quenched in the $\Pi^{\text{lower}}(1_1, n=0)$ and $\Pi^{\text{upper}}(1_1, n=0)$ states.[12] This behavior will be observed in general for the E states, i.e., the NH_3 subunit will be relatively freely inverting in the Σ states of the complex, but the inversion will be quenched in those states with $\Omega>0$. As in the case with all the A states, only mixing through the potential or through the Coriolis interaction will quench the subunit inversion in the Σ states of E symmetry. The inversion splitting of the Σ states of E symmetry decreases as the energy increases. It is about 22 GHz in the $j_k=1_1$, $n=0$ Σ states, and it drops to about 18 GHz for the $j_k=1_1$, $n=1$ Σ states, and further drops to about 14 GHz in the $j_k=2_1$, $n=0$ Σ states. This is a result of increased mixing with states that have the opposite inversion–tunneling symmetry. Furthermore, as the energy increases, so does the density of states, which leads to increased mixing among the states with a concomitant decrease in the inversion splitting.

Table X displays all bound levels of Ar–NH_3 with $J\leqslant 2$ obtained from this IPS. Eight radial functions were used when calculating the energy levels shown in Tables IX and X to ensure accurate results near the dissociation limit. Table XI reports the largest contributions of basis states to several of the low lying eigenstates with $J=2$. As the dissociation limit is approached, there is a much higher density of states, and it becomes almost meaningless to use labels based on the dominant free rotor state due to the large amount of mixing. Coriolis interactions perturb and mix levels that correlate to the same free rotor state but have values of Ω that differ by one. Angular-radial coupling implies a mixing of states with

TABLE IX. Predicted energies in cm^{-1} for bound vibrational states of Ar–ND_3 with $0\leqslant J\leqslant 2$. The labels indicate the dominant free rotor contribution to the eigenstate, and become more qualitative at higher energies. The full rovibrational symmetry is designated. The model uncertainty is roughly 1 GHz (0.03 cm^{-1}) for the vibrational levels, but the relative uncertainty for the rotational levels for any given state is only 5 MHz.

	$J=0$	$J=1$	$J=2$
A_1' vibrational symmetry state			
$\Sigma^s(0_0, n=0)$	104.3333	−104.1576	−103.8060
$\Pi^a(1_0, n=0)$		−96.2436	−95.8997
$\Sigma^a(1_0, n=0)$	−84.1926	−84.0187	−83.6709
$\Delta^s(2_0, n=0)$			−77.5671
$\Sigma^s(0_0, n=1)$	−75.3048	−75.1452	−74.8261
$\Pi^a(1_0, n=1)$		−70.2158	−69.9018
$\Pi^s(2_0, n=0)/\Pi^{\text{lower}}(3_3, n=0)$		−65.6367	−65.3545
$\Sigma^s(2_0, n=0)$	−63.7738	−63.5748	−63.1802
$\Pi^{\text{lower}}(3_3, n=0)/\Delta^{\text{lower}}(3_3, n=0)$		−61.5623	−61.5724
$\Delta^{\text{lower}}(3_3, n=0)/\Pi^{\text{lower}}(3_3, n=0)$			−60.9554
$\Sigma^s(3_3, n=0)$	−57.4684	−57.2642	−56.8571
$\Sigma^a(1_0, n=1)$	−54.6031	−54.4512	−54.1477
$\Delta^{\text{upper}}(3_3, n=0)$			−52.7021
$\Pi^{\text{upper}}(3_3, n=0)$		−52.0480	−51.6131
$\Sigma^s(0_0, n=2)$	−46.1275	−45.9732	−45.6656
$\Delta^s(2_0, n=1)$			−45.4247
$\Pi^a(1_0, n=2)$		−42.6314	−42.3311
$\Pi^a(3_0, n=0)$		−37.8239	−37.5937
$\Sigma^s(2_0, n=1)$	−35.3190	−35.1221	−34.7490
$\Delta^a(3_0, n=0)$			−34.6701
$\Sigma^a(1_0, n=2)/\Sigma^s(0_0, n=3)$	−33.4862	−33.3570	−33.0960
$\Sigma^s(0_0, n=3)/\Sigma^s(3_0, n=0)$	−32.3186	−32.2004	−31.9568
$\Pi^a(3_0, n=0)/\Pi^s(2_0, n=1)$		−30.0179	−29.6592
$\Delta^{\text{lower}}(3_3, n=1)$			−29.3261
$\Sigma^a(1_0, n=2)/\Sigma^s(2_0, n=2)$	−27.8784	−27.6645	−27.2351
$\Pi^a(1_0, n=3)/\Pi^{\text{lower}}(3_3, n=1)$		−24.6950	−24.4587
$\Delta^{\text{upper}}(3_3, n=1)$			−22.9834
$\Sigma^s(3_3, n=1)/\Sigma^s(0_0, n=4)$	−21.7140	−21.5799	−21.3121
$\Delta^{\text{lower}}(4_3, n=0)$			−18.2019
$\Pi^a(1_0, n=3)/\Pi^{\text{upper}}(3_3, n=1)$		−18.1895	−17.9234
$\Sigma^s(0_0, n=4)/\Sigma^a(1_0, n=3)$	−16.5971	−16.4918	−16.2587
$\Pi^{\text{lower}}(4_3, n=0)$		−16.0333	−15.7008
$\Delta^{\text{lower}}(4_3, n=0)/\Delta^a(3_0, n=1)$			−15.1608
$\Sigma^a(1_0, n=3)/\Sigma^a(4_3, n=0)$	−13.2241	−13.1281	−12.9369
$\Pi^{\text{upper}}(4_3, n=0)$		−11.7040	−11.6572
$\Sigma^a(4_3, n=0)$	−11.6506	−11.0349	−10.7533
$\Delta^{\text{upper}}(4_3, n=0)$			−10.1052
$\Pi^s(2_0, n=2)/\Pi^{\text{lower}}(3_3, n=2)$		−10.1845	−9.7650
$\Sigma^a(4_3, n=0)/\Sigma^s(0_0, n=4)$	−7.9545	−7.7933	−7.4695
$\Pi^a(1_0, n=4)$		−6.9842	−6.7674
$\Sigma^s(0_0, n=5)$	−6.3165	−6.2100	−5.9984
$\Delta^a(3_0, n=1)$			−5.5994
$\Delta^{\text{lower}}(3_3, n=2)$			−3.4685
$\Sigma^a(3_0, n=1)/\Pi^a(3_0, n=1)$	−2.6879	−2.6325	−2.4824
$\Pi^{\text{upper}}(3_3, n=2)$		−2.4259	−2.0542
$\Pi^a(3_0, n=1)$		−1.6046	−1.2761
$\Sigma^a(1_0, n=4)$	−0.3258	−0.1310	0.2560
A_1'' vibrational symmetry state			
$\Pi^a(1_0, n=0)$		−96.2395	−95.8875
$\Delta^s(2_0, n=0)$			−77.5670
$\Pi^a(1_0, n=1)$		−70.2142	−69.8973
$\Pi^s(2_0, n=0)/\Pi^{\text{lower}}(3_3, n=0)$		−65.6550	−65.4057
$\Sigma^a(3_3, n=0)$	−63.1165	−62.9056	−62.4901
$\Pi^{\text{lower}}(3_3, n=0)/\Delta^{\text{lower}}(3_3, n=0)$		−61.5251	−61.5249
$\Delta^{\text{lower}}(3_3, n=0)/\Pi^{\text{lower}}(3_3, n=0)$			−60.8923
$\Delta^{\text{upper}}(3_3, n=0)$			−52.7022
$\Pi^{\text{upper}}(3_3, n=0)$		−52.0435	−51.5999
$\Delta^s(2_0, n=1)$			−45.4255
$\Pi^a(1_0, n=2)$		−42.6271	−42.3184
$\Pi^a(3_0, n=0)$		−37.7857	−37.4829

TABLE IX. (*Continued.*)

	$J=0$	$J=1$	$J=2$
A_1'' vibrational symmetry state			
$\Delta^a(3_0, n=0)$			−34.6853
$\Sigma^a(3_3, n=1)$	−31.3475	−31.2114	−30.9358
$\Pi^a(3_0, n=0)/\Pi^s(2_0, n=1)$		−30.0124	−29.6561
$\Delta^{lower}(3_3, n=1)$			−29.2920
$\Pi^a(1_0, n=3)/\Pi^{lower}(3_3, n=1)$		−24.6823	−24.4229
$\Delta^{upper}(3_3, n=1)$			−22.9815
$\Delta^{lower}(4_3, n=0)$			−18.2024
$\Pi^a(1_0, n=3)/\Pi^{upper}(3_3, n=1)$		−18.1733	−17.8780
$\Pi^{lower}(4_3, n=0)$		−16.1181	−15.8999
$\Delta^{lower}(4_3, n=0)/\Delta^a(3_0, n=1)$			−15.1871
$\Sigma^s(4_3, n=0)$	−12.7634	−12.6461	−12.3984
$\Pi^{upper}(4_3, n=0)/\Delta^{upper}(4_3, n=0)$		−11.1934	−11.0440
$\Delta^{upper}(4_3, n=0)/\Pi^{upper}(4_3, n=0)$			−10.1275
$\Pi^s(2_0, n=2)/\Pi^{lower}(3_3, n=2)$		−10.1274	−9.6150
$\Pi^{upper}(3_3, n=2)$		−6.9946	−6.7995
$\Delta^a(3_0, n=1)$			−5.6013
$\Delta^{lower}(3_3, n=2)$			−3.4653
$\Sigma^a(3_3, n=2)$	−3.4643	−3.3143	−3.0156
$\Pi^a(3_0, n=1)$		−2.4281	−2.0638
$\Pi^{upper}(3_3, n=2)$		−1.6181	−1.2762
A_2' vibrational symmetry state			
$\Pi^s(1_0, n=0)$		−96.2893	−95.9373
$\Delta^a(2_0, n=0)$			−77.5165
$\Pi^s(1_0, n=1)$		−70.2298	−69.9135
$\Pi^a(2_0, n=0)/\Pi^{lower}(3_3, n=0)$		−65.6482	−65.4000
$\Sigma^s(3_3, n=0)$	−63.1683	−62.9563	−62.5389
$\Pi^{lower}(3_3, n=0)/\Delta^{lower}(3_3, n=0)$		−61.4850	−61.5075
$\Delta^{lower}(3_3, n=0)/\Pi^{lower}(3_3, n=0)$			−60.8726
$\Delta^{upper}(3_3, n=0)$			−52.7010
$\Pi^{upper}(3_3, n=0)$		−52.0782	−51.6321
$\Delta^a(2_0, n=1)$			−45.3989
$\Pi^s(1_0, n=2)$		−42.6465	−42.3381
$\Pi^s(3_0, n=0)$		−37.8090	−37.5056
$\Delta^s(3_0, n=0)$			−34.7081
$\Sigma^s(3_3, n=1)$	−31.3910	−31.2533	−30.9748
$\Pi^s(3_0, n=0)/\Pi^a(2_0, n=1)$		−30.0027	−29.6302
$\Delta^{lower}(3_3, n=1)$			−29.3172
$\Pi^s(1_0, n=3)/\Pi^{lower}(3_3, n=1)$		−24.7128	−24.4526
$\Delta^{upper}(3_3, n=1)$			−22.9916
$\Delta^{lower}(4_3, n=0)$			−18.1935
$\Pi^s(1_0, n=3)/\Pi^{upper}(3_3, n=1)$		−18.1995	−17.9010
$\Pi^{lower}(4_3, n=0)$		−16.1050	−15.8838
$\Delta^{lower}(4_3, n=0)/\Delta^s(3_0, n=1)$			−15.1856
$\Sigma^a(4_3, n=0)$	−12.7299	−12.6185	−12.3804
$\Pi^{upper}(4_3, n=0)/\Delta^{upper}(4_3, n=0)$		−11.2071	−11.0438
$\Delta^{upper}(4_3, n=0)/\Pi^{upper}(4_3, n=0)$			−10.1373
$\Pi^a(2_0, n=2)/\Pi^{lower}(3_3, n=2)$		−10.1245	−9.6012
$\Pi^{upper}(3_3, n=2)$		−7.0334	−6.8378
$\Delta^s(3_0, n=1)$			−5.6068
$\Delta^{lower}(3_3, n=2)$			−3.4424
$\Sigma^s(3_3, n=2)$	−3.5009	−3.3508	−3.0521
$\Pi^s(3_0, n=1)$		−2.3999	−2.0360
$\Pi^{upper}(3_3, n=2)$		−1.6337	−1.2903
A_2'' vibrational symmetry state			
$\Sigma^a(0_0, n=0)$	−104.2865	−104.1107	−103.7592
$\Pi^s(1_0, n=0)$		−96.2934	−95.9495
$\Sigma^s(1_0, n=0)$	−84.2289	−84.0550	−83.7073
$\Delta^a(2_0, n=0)$			−77.5165
$\Sigma^a(0_0, n=1)$	−75.2582	−75.0986	−74.7795
$\Pi^s(1_0, n=1)$		−70.2311	−69.9169
$\Pi^a(2_0, n=0)/\Pi^{lower}(3_3, n=0)$		−65.6291	−65.3468
$\Sigma^a(2_0, n=0)$	−63.7395	−63.5406	−63.1461
$\Pi^{lower}(3_3, n=0)/\Delta^{lower}(3_3, n=0)$		−61.5221	−61.5510

TABLE IX. (*Continued.*)

	$J=0$	$J=1$	$J=2$
A_2'' vibrational symmetry state			
$\Delta^{lower}(3_3, n=0)/\Pi^{lower}(3_3, n=0)$			−60.9392
$\Sigma^a(3_3, n=0)$	−57.4243	−57.2206	−56.8144
$\Sigma^s(1_0, n=1)$	−54.6124	−54.4603	−54.1565
$\Delta^{upper}(3_3, n=0)$			−52.7008
$\Pi^{upper}(3_3, n=0)$		−52.0824	−51.6444
$\Sigma^a(0_0, n=2)$	−46.1007	−45.9464	−45.6385
$\Delta^a(2_0, n=1)$			−45.3981
$\Pi^s(1_0, n=2)$		−42.6507	−42.3504
$\Pi^s(3_0, n=0)$		−37.8475	−37.6175
$\Sigma^a(2_0, n=1)$	−35.3079	−35.1106	−34.7473
$\Delta^s(3_0, n=0)$			−34.6822
$\Sigma^s(1_0, n=2)/\Sigma^a(0_0, n=3)$	−33.5009	−33.3708	−33.1081
$\Sigma^a(0_0, n=3)/\Sigma^a(3_0, n=0)$	−32.3050	−32.1887	−31.9481
$\Pi^s(3_0, n=0)/\Pi^a(2_0, n=1)$		−30.0049	−29.6287
$\Delta^{lower}(3_3, n=1)$			−29.3425
$\Sigma^s(1_0, n=2)/\Sigma^a(2_0, n=2)$	−27.8739	−27.6643	−27.2428
$\Pi^s(1_0, n=3)/\Pi^{lower}(3_3, n=1)$		24.7251	−24.4873
$\Delta^{upper}(3_3, n=1)$			−22.9934
$\Sigma^a(3_3, n=1)/\Sigma^a(0_0, n=4)$	−21.6842	−21.5505	−21.2835
$\Delta^{lower}(4_3, n=0)$			−18.1942
$\Pi^s(1_0, n=3)/\Pi^{upper}(3_3, n=1)$		−18.2157	−17.9452
$\Sigma^a(0_0, n=4)/\Sigma^s(1_0, n=3)$	−16.5921	−16.4868	−16.2534
$\Pi^{lower}(4_3, n=0)$		−16.0210	−15.6868
$\Delta^{lower}(4_3, n=0)/\Delta^s(3_0, n=1)$			−15.1596
$\Sigma^s(1_0, n=3)/\Sigma^s(4_3, n=0)$	−13.2186	−13.1230	−12.9323
$\Pi^{upper}(4_3, n=0)$		−11.7121	−11.6609
$\Sigma^s(4_3, n=0)$	−11.6618	−11.0535	−10.7616
$\Delta^{upper}(4_3, n=0)$			−10.1191
$\Pi^a(2_0, n=2)/\Pi^{lower}(3_3, n=2)$		−10.1832	−9.7548
$\Sigma^s(4_3, n=0)/\Sigma^a(0_0, n=4)$	−7.9391	−7.7789	−7.4574
$\Pi^s(1_0, n=4)$		−7.0224	−6.8039
$\Sigma^a(0_0, n=5)$	−6.2797	−6.1737	−5.9631
$\Delta^s(3_0, n=1)$			−5.6048
$\Delta^{lower}(3_3, n=2)$			−3.4461
$\Sigma^s(3_0, n=1)/\Pi^s(3_0, n=1)$	−2.7121	−2.6532	−2.4994
$\Pi^{upper}(3_3, n=2)$		−2.4000	−2.0304
$\Pi^s(3_0, n=1)$		−1.6220	−1.2951
$\Sigma^s(1_0, n=4)$	−0.3580	−0.1629	0.2249
E' vibrational symmetry state			
$\Sigma^s(1_1, n=0)$	−99.1325	−98.9686	−98.6405
$\Pi^{lower}(1_1, n=0)$		−97.2378	−96.8649
$\Pi^{upper}(1_1, n=0)$		−93.2556	−92.9075
$\Pi^{lower}(2_2, n=0)$		−82.6802	−82.5078
$\Sigma^s(2_2, n=0)$	−82.4840	−82.2133	−81.7823
$\Delta^{lower}(2_2, n=0)$			−80.7459
$\Delta^{lower}(2_1, n=0)$			−79.6963
$\Pi^{upper}(2_2, n=0)$		−79.3036	−78.9406
$\Delta^{upper}(2_1, n=0)$			−72.3674
$\Sigma^a(2_1, n=0)$	−71.4453	−71.3406	−71.1154
$\Pi^{lower}(2_1, n=0)$		−70.0567	−69.6361
$\Delta^{upper}(2_2, n=0)$			−69.1131
$\Pi^{upper}(2_1, n=0)$		−68.9955	−68.6046
$\Pi^{lower}(1_1, n=1)$		−64.9732	−64.6533
$\Sigma^s(1_1, n=1)/\Sigma^a(2_1, n=0)$	−62.2576	−62.0909	−61.7577
$\Pi^{upper}(1_1, n=1)$		−57.8844	−57.5528
$\Sigma^s(2_2, n=0)$	−53.4767	−53.4499	−53.3029
$\Pi^{lower}(2_2, n=1)$		−52.8750	−52.4327
$\Delta^{lower}(3_3, n=0)/\Delta^{lower}(2_2, n=1)/\Delta^{lower}(2_2, n=1)$			−51.8348
$\Pi^{upper}(2_2, n=1)$		−50.1584	−49.9336
$\Delta^{lower}(2_1, n=1)$			−49.6390
$\Delta^{lower}(2_2, n=1)/\Delta^{lower}(3_2, n=0)$			−47.0090
$\Delta^{lower}(3_1, n=0)$			−45.3235
$\Pi^{lower}(3_2, n=0)$		−45.5274	−45.2267
$\Sigma^a(2_1, n=1)$	−43.5773	−43.4449	−43.1772

TABLE IX. (*Continued.*)

	$J=0$	$J=1$	$J=2$
E' vibrational symmetry state			
$\Delta^{upper}(2_1, n=1)$			−42.2624
$\Pi^{lower}(2_1, n=1)/\Pi^{lower}(3_1, n=0)$		−42.1183	−41.7635
$\Sigma^s(1_1, n=2)/\Sigma^a(3_2, n=0)$	−41.9712	−41.8593	−41.5533
$\Pi^{upper}(2_1, n=1)$		−41.5739	−41.2110
$\Pi^{upper}(3_2, n=0)/\Pi^{lower}(3_1, n=0)$		−40.6328	−40.2552
$\Delta^{lower}(3_2, n=0)/\Delta^{lower}(3_1, n=0)$			−39.8641
$\Pi^{lower}(1_1, n=2)$		−39.5041	−39.1961
$\Sigma^s(3_1, n=0)/\Sigma^s(4_4, n=0)$	−38.0049	−37.8743	−37.6103
$\Delta^{upper}(2_2, n=1)$			−36.9862
$\Pi^{lower}(3_1, n=0)$		−36.2972	−36.0050
$\Pi^{upper}(3_1, n=0)$		−34.9436	−34.6403
$\Delta^{upper}(3_1, n=0)$			−34.5987
$\Delta^{lower}(4_4, n=0)$			−32.0434
$\Sigma^s(4_4, n=0)/\Sigma^s(3_1, n=0)$	−32.2131	−32.0462	−31.7103
$\Pi^{lower}(4_4, n=0)$		−31.0083	−30.5754
$\Pi^{upper}(1_1, n=2)/\Pi^{upper}(2_1, n=2)$		−30.0809	−29.7636
$\Sigma^a(2_1, n=2)/\Sigma^s(4_4, n=0)$	−29.4381	−29.2339	−28.8311
$\Pi^{upper}(4_4, n=0)$		−27.5129	−27.3077
$\Sigma^s(1_1, n=3)/\Sigma^s(2_2, n=2)$	−27.4476	−27.2182	−26.8231
$\Delta^{lower}(2_1, n=2)/\Delta^{upper}(4_4, n=0)$			−25.0754
$\Delta^{upper}(4_4, n=0)$			−24.4373
$\Delta^{upper}(2_1, n=2)$			−22.6524
$\Sigma^a(2_1, n=2)/\Sigma^s(1_1, n=3)$	−19.1885	−19.0467	−18.7634
$\Delta^{lower}(2_2, n=2)/\Delta^{lower}(3_2, n=1)$			−18.7424
$\Delta^{upper}(2_2, n=2)$			−17.1999
$\Sigma^a(3_2, n=1)$	−16.2902	−16.1395	−15.8382
$\Delta^{lower}(3_2, n=1)$			−14.3579
$\Delta^{upper}(3_2, n=1)$			−10.9975
$\Sigma^s(2_2, n=3)/\Sigma^a(2_1, n=2)$	−10.4310	−10.2858	−9.9955
$\Sigma^s(1_1, n=4)$	−8.6041	−8.4776	−8.2247
$\Sigma^s(3_1, n=1)$	−4.8542	−4.7041	−4.4040
$\Sigma^s(2_2, n=3)$	−4.1680	−4.0323	−3.7613
E'' vibrational symmetry state			
$\Sigma^a(1_1, n=0)$	−99.0827	−98.9190	−98.5911
$\Pi^{lower}(1_1, n=0)$		−97.2377	−96.8647
$\Pi^{upper}(1_1, n=0)$		−93.2555	−92.9073
$\Pi^{lower}(2_2, n=0)$		−82.6663	−82.4876
$\Sigma^a(2_2, n=0)$	−82.4331	−82.1771	−81.7538
$\Delta^{lower}(2_2, n=0)$			−80.7459
$\Delta^{lower}(2_1, n=0)$			−79.6963
$\Pi^{upper}(2_2, n=0)$		−79.3029	−78.9384
$\Delta^{upper}(2_1, n=0)$			−72.3674
$\Sigma^s(2_1, n=0)$	−71.4575	−71.3537	−71.1298
$\Pi^{lower}(2_1, n=0)$		−70.0544	−69.6298
$\Delta^{upper}(2_2, n=0)$			−69.1131
$\Pi^{upper}(2_1, n=0)$		−68.9968	−68.6083
$\Pi^{lower}(1_1, n=1)$		−64.9730	−64.6528
$\Sigma^a(1_1, n=1)/\Sigma^s(2_1, n=0)$	−62.2420	−62.0756	−61.7430
$\Pi^{upper}(1_1, n=1)$		−57.8843	−57.5526
$\Sigma^a(2_2, n=0)$	−53.4467	−53.4252	−53.2802
$\Pi^{lower}(2_2, n=1)$		−52.8703	−52.4272
$\Delta^{lower}(3_2, n=0)/\Delta^{lower}(2_2, n=1)/\Delta^{lower}(2_2, n=1)$			−51.8348
$\Pi^{upper}(2_2, n=1)$		−50.1578	−49.9324
$\Delta^{lower}(2_1, n=1)$			−49.6384
$\Delta^{lower}(2_2, n=1)/\Delta^{lower}(3_2, n=0)$			−47.0090
$\Delta^{lower}(3_1, n=0)$			−45.3234
$\Pi^{lower}(3_2, n=0)$		−45.5277	−45.2278
$\Sigma^s(2_1, n=1)$	−43.5923	−43.4592	−43.1902
$\Delta^{upper}(2_1, n=1)$			−42.2631
$\Pi^{lower}(2_1, n=1)/\Pi^{lower}(3_1, n=0)$		−42.1224	−41.7735
$\Sigma^a(1_1, n=2)/\Sigma^s(3_2, n=0)$	−41.9695	−41.8512	−41.5354
$\Pi^{upper}(2_1, n=1)$		−41.5743	−41.2110
$\Pi^{upper}(3_2, n=0)/\Pi^{lower}(3_1, n=0)$		−40.6340	−40.2585

TABLE IX. (*Continued.*)

	$J=0$	$J=1$	$J=2$
E' vibrational symmetry state			
$\Delta^{lower}(3_2, n=0)/\Delta^{lower}(3_1, n=0)$			−39.8642
$\Pi^{lower}(1_1, n=2)$		−39.5037	−39.1953
$\Sigma^a(3_1, n=0)/\Sigma^a(4_4, n=0)$	−37.9680	−37.8405	−37.5819
$\Delta^{upper}(2_2, n=1)$			−36.9863
$\Pi^{lower}(3_1, n=0)$		−36.2956	−36.0010
$\Pi^{upper}(3_1, n=0)$		−34.9423	−34.6394
$\Delta^{upper}(3_1, n=0)$			−34.5958
$\Delta^{lower}(4_4, n=0)$			−32.0434
$\Sigma^a(4_4, n=0)/\Sigma^a(3_1, n=0)$	−32.1756	−32.0103	−31.6778
$\Pi^{lower}(4_4, n=0)$		−31.0089	−30.5763
$\Pi^{upper}(1_1, n=2)/\Pi^{upper}(2_1, n=2)$		−30.0788	−29.7588
$\Sigma^s(2_1, n=2)/\Sigma^a(4_4, n=0)$	−29.4204	−29.2185	−28.8194
$\Pi^{upper}(4_4, n=0)$		−27.5050	−27.2953
$\Sigma^a(1_1, n=3)/\Sigma^a(2_2, n=2)$	−27.4097	−27.1868	−26.7935
$\Delta^{lower}(2_1, n=2)/\Delta^{upper}(4_4, n=0)$			−25.0753
$\Delta^{upper}(4_4, n=0)$			−24.4372
$\Delta^{upper}(2_1, n=2)$			−22.6524
$\Delta^{lower}(2_2, n=2)/\Delta^{lower}(3_2, n=1)$			−18.7426
$\Sigma^s(2_1, n=2)/\Sigma^a(1_1, n=3)$	−19.1672	−19.0253	−18.7417
$\Delta^{upper}(2_2, n=2)$			−17.1999
$\Sigma^s(3_2, n=1)$	−16.3015	−16.1508	−15.8496
$\Delta^{lower}(3_2, n=1)$			−14.3579
$\Delta^{upper}(3_2, n=1)$			−10.9975
$\Sigma^a(2_2, n=3)/\Sigma^s(2_1, n=2)$	−10.4299	−10.2848	−9.9947
$\Sigma^a(1_1, n=4)$	−8.5598	−8.4332	−8.1803
$\Sigma^a(3_1, n=1)$	−4.8374	−4.6873	−4.3871
$\Sigma^a(2_2, n=3)$	−4.1217	−3.9861	−3.7153

the same value of Ω, and does not depend on the free rotor state that the level correlates with. The IPS itself mixes the free rotor states and is of course the explicit source of the angular-radial coupling. Due to the large amount of mixing, it can be quite difficult to label the vibrational states because there is often not any single basis state that dominates the eigenstate.

It is found that the eigenvectors are typically about 90% pure with respect to the angular basis for the *ortho* states as well as the lowest few *para* states. That is, for a given eigenvector, the sum of the squared coefficients of the basis states with identical angular dependence (but with possibly more than one radial basis state) is about 0.90. This indicates that the IPS is not significantly mixing the free rotor states of the monomer in these eigenstates. There is significant mixing of the angular basis of the *para* states starting at energies as low as 30 cm^{-1} above the ground state. For example, the $\Sigma_a(2_2, n=0)$ state has about 25% $\Sigma_a(1_1, n=1)$ character. This results from the fact that the energy for free internal rotor 2_2 states is 28 cm^{-1} above the free internal rotor 1_1 levels, while the vdW stretching frequency is about 34 cm^{-1}. Therefore, the zero-order energies of these levels are quite close to each other, and the V_{33} term in the potential mixes them substantially.

Another important consequence of the high degree of mixing in E states is that the ordering of the parity components of a state with $\Omega>0$ can be reversed relative to that expected in the absence of anisotropy in the IPS. In particular, the E' component of the $\Pi^{lower}(1_1, n=1)$ state lies

TABLE X. Predicted energies in cm^{-1} for bound vibrational states of Ar–NH_3 with $0 \leq J \leq 2$. The labels indicate the dominant free rotor contribution to the eigenstate, and become more qualitative at higher energies. The full rovibrational symmetry is designated. The model uncertainty is roughly 1 GHz (0.03 cm^{-1}) for the vibrational levels, but the relative uncertainty for the rotational levels for any given state is only 5 MHz.

	$J=0$	$J=1$	$J=2$
A_2' vibrational symmetry state			
$\Pi(1_0, n=0)$		−84.0842	−83.6985
$\Pi(1_0, n=1)$		−52.4009	−52.0433
$\Delta(2_0, n=0)$			−45.2822
$\Pi(2_0, n=0)$		−34.2663	−33.8883
$\Pi(1_0, n=1)$		−26.4428	−26.1305
$\Delta^{\text{lower}}(3_3, n=0)$			−19.5083
$\Sigma^s(3_3, n=0)$	−19.3507	−19.2319	−18.9481
$\Pi^{\text{lower}}(3_3, n=0)$		−17.8027	−17.2626
$\Pi^{\text{upper}}(3_3, n=0)/\Delta(2_0, n=1)$		−12.0658	−11.9143
$\Delta(2_0, n=1)/\Delta^{\text{upper}}(3_3, n=0)/\Pi^{\text{upper}}(3_3, n=0)$			−11.3101
$\Pi(1_0, n=2)$		−6.7871	−6.4927
$\Delta^{\text{upper}}(3_3, n=0)$			−5.3490
$\Pi(2_0, n=1)$		−0.7118	−0.3764
A_2'' vibrational symmetry state			
$\Sigma(0_0, n=0)$	−100.6972	−100.5054	−100.1218
$\Pi(1_0, n=0)$		−84.0902	−83.7164
$\Sigma(1_0, n=0)$	−74.2358	−74.0477	−73.6716
$\Sigma(0_0, n=1)$	−66.4030	−66.2245	−65.8676
$\Pi(1_0, n=1)$		−52.4067	−52.0607
$\Delta(2_0, n=0)$			−45.2823
$\Sigma(0_0, n=2)$	−45.5188	−45.3518	−45.0179
$\Sigma(1_0, n=1)$	−39.9264	−39.7592	−39.4247
$\Pi(2_0, n=0)$		−34.3268	−34.0627
$\Sigma(2_0, n=0)$	−32.1440	−31.9010	−31.4224
$\Pi(1_0, n=2)$		−26.4414	−26.1262
$\Sigma(0_0, n=3)$	−24.8648	−24.7242	−24.4430
$\Delta^{\text{lower}}(3_3, n=0)$			−19.4956
$\Pi^{\text{lower}}(3_3, n=0)$		−18.0637	−17.8493
$\Sigma(1_0, n=2)$	−17.9055	−17.5667	−17.0535
$\Sigma^a(3_3, n=0)/\Pi^{\text{upper}}(3_3, n=0)$	−13.6913	−13.5256	−13.1956
$\Pi^{\text{upper}}(3_3, n=0)/\Sigma^a(3_3, n=0)$		−12.0829	−11.9379
$\Delta^{\text{lower}}(3_3, n=0)$			−11.3387
$\Sigma(0_0, n=4)/\Sigma^a(3_3, n=0)$	−9.8334	−9.6900	−9.3999
$\Pi(1_0, n=3)$		−6.7994	−6.5290
$\Delta^{\text{upper}}(3_3, n=0)$			−5.3489
$\Sigma(0_0, n=4)$	−3.0582	−2.9427	−2.7118
$\Sigma(2_0, n=1)$	−1.8457	−1.7367	−1.5026
$\Pi(2_0, n=1)$		−0.6625	−0.2461
E' vibrational symmetry state			
$\Sigma^s(1_1, n=0)$	−88.2963	−88.1282	−87.7901
$\Pi^{\text{lower}}(1_1, n=0)$		−86.5711	−86.1407
$\Pi^{\text{upper}}(1_1, n=0)$		−79.7379	−79.3572
$\Sigma^s(2_2, n=0)$	−62.0218	−61.9464	−61.7227
$\Pi^{\text{lower}}(2_2, n=0)$		−61.4130	−60.9276
$\Pi^{\text{upper}}(2_2, n=0)$		−56.8384	−56.4836
$\Delta^{\text{lower}}(2_2, n=0)$			−55.8139
$\Sigma^s(1_1, n=1)$	−52.4914	−52.3009	−51.9199
$\Delta^{\text{lower}}(2_1, n=0)$			−50.5286
$\Pi^{\text{lower}}(1_1, n=1)$		−50.5409	−50.1756
$\Pi^{\text{upper}}(1_1, n=1)$		−48.7124	−48.3545
$\Delta^{\text{upper}}(2_2, n=0)$			−44.3138
$\Delta^{\text{upper}}(2_1, n=0)$			−42.8566
$\Pi^{\text{lower}}(2_1, n=0)$		−41.7169	−41.3590
$\Sigma^a(2_1, n=0)$	−37.4993	−37.4512	−37.2485
$\Pi^{\text{upper}}(2_1, n=0)$		−36.7679	−36.2125
$\Sigma^s(1_1, n=2)/\Sigma^s(2_2, n=1)$	−31.7785	−31.6149	−31.2874
$\Pi^{\text{lower}}(1_1, n=2)$		−28.5521	−28.2384
$\Pi^{\text{lower}}(2_2, n=1)/\Pi^{\text{lower}}(1_1, n=2)$		−27.8022	−27.4638
$\Delta^{\text{lower}}(2_2, n=1)$			−23.0229
$\Sigma^s(2_2, n=1)/\Sigma^s(1_1, n=2)$	−21.7828	−21.6264	−21.3120
$\Pi^{\text{upper}}(1_1, n=2)$		−21.0651	−20.6962
$\Pi^{\text{upper}}(2_2, n=1)$		−19.7951	−19.4601
$\Delta^{\text{lower}}(2_1, n=1)$			−17.2010
$\Delta^{\text{upper}}(2_2, n=1)$			−13.3272
$\Delta^{\text{upper}}(2_1, n=1)$			−11.6977
$\Sigma^s(1_1, n=3)$	−11.0361	−10.9265	−10.6957
$\Pi^{\text{lower}}(1_1, n=3)/\Pi^{\text{lower}}(2_1, n=1)$		−10.3861	−10.0425
$\Pi^{\text{lower}}(2_1, n=1)$		−9.5674	−9.1983
$\Pi^{\text{upper}}(1_1, n=3)$		−7.6507	−7.3568
$\Sigma^a(2_1, n=1)$	−4.8375	−4.6725	−4.3431
$\Pi^{\text{upper}}(2_1, n=1)$		−1.6991	−1.3988
$\Sigma^s(2_2, n=2)/\Sigma^s(1_1, n=3)$	−0.0029	0.0990	0.3117
E'' vibrational symmetry state			
$\Sigma^a(1_1, n=0)$	−87.5318	−87.3777	−87.0606
$\Pi^{\text{lower}}(1_1, n=0)$		−86.5584	−86.1092
$\Pi^{\text{upper}}(1_1, n=0)$		−79.7367	−79.3536
$\Pi^{\text{lower}}(2_2, n=0)$		−61.5809	−61.3254
$\Sigma^a(2_2, n=0)$	−61.2540	−61.0119	−60.5609
$\Pi^{\text{upper}}(2_2, n=0)$		−56.8371	−56.4797
$\Delta^{\text{lower}}(2_2, n=0)$			−55.8140
$\Sigma^a(1_1, n=1)$	−51.8841	−51.6949	−51.3166
$\Delta^{\text{lower}}(2_1, n=0)$			−50.5286
$\Pi^{\text{lower}}(1_1, n=1)$		−50.5428	−50.1813
$\Pi^{\text{upper}}(1_1, n=1)$		−48.7096	−48.3459
$\Delta^{\text{upper}}(2_2, n=0)$			−44.3137
$\Delta^{\text{upper}}(2_1, n=0)$			−42.8566
$\Pi^{\text{lower}}(2_1, n=0)$		−41.7217	−41.3732
$\Sigma^s(2_1, n=0)$	−37.9906	−37.8529	−37.5614
$\Pi^{\text{upper}}(2_1, n=0)$		−36.8516	−36.3731
$\Sigma^a(1_1, n=2)/\Sigma^a(2_2, n=1)$	−31.1077	−30.9449	−30.6191
$\Pi^{\text{lower}}(1_1, n=2)$		−28.5424	−28.2098
$\Pi^{\text{lower}}(2_2, n=1)/\Pi^{\text{lower}}(1_1, n=2)$		−27.8114	−27.4909
$\Delta^{\text{lower}}(2_2, n=1)$			−23.0230
$\Pi^{\text{upper}}(1_1, n=2)$		−21.0821	−20.7457
$\Sigma^a(2_2, n=1)/\Sigma^a(1_1, n=2)$	−21.1087	−20.9506	−20.6333
$\Pi^{\text{upper}}(2_2, n=1)$		−19.7800	−19.4155
$\Delta^{\text{lower}}(2_1, n=1)$			−17.2009
$\Delta^{\text{upper}}(2_2, n=1)$			−13.3272
$\Delta^{\text{upper}}(2_1, n=1)$			−11.6976
$\Sigma^a(1_1, n=3)$	−10.7205	−10.7095	−10.5470
$\Pi^{\text{lower}}(1_1, n=3)/\Pi^{\text{lower}}(2_1, n=1)$		−10.2727	−9.8379
$\Pi^{\text{lower}}(2_1, n=1)$		−9.5799	−9.2296
$\Pi^{\text{upper}}(1_1, n=3)$		−7.6485	−7.3501
$\Sigma^s(2_1, n=1)$	−5.0066	−4.8438	−4.5184
$\Pi^{\text{upper}}(2_1, n=1)$		−1.7011	−1.4050

higher in energy than the E'' component,[15] even though the $\Pi^{\text{lower}}(1_1, n=1)$ state is only 32 GHz above the $\Sigma^a(1_1, n=1)$ state (E'' symmetry), while it is 50 GHz above the $\Sigma^s(1_1, n=1)$ state (E' symmetry). A two level Coriolis analysis would predict that the E'' component of the Π state should lie above the E' component. As seen in Table XI, the $\Sigma 1_1$ and Π_1^1 levels with $n=1$ are all highly mixed, and a two level treatment is not appropriate in this case.

B. Comparisons with other work

There are two published *ab initio* studies of the Ar–NH_3 complex.[19,20] In both of these the global minimum is found

TABLE XI. Contribution of angular basis functions to several experimentally observed low lying eigenstates. The modulus squared for all radial contributions with a given angular function are summed and reported in this table. The notation for the angular functions is: Σ, Π, or Δ for $\Omega=0$, 1, or 2 respectively, followed by a (+) or (−) superscript to indicate ϵ, then j_k, followed by a (+) or (−) superscript to indicate ξ (for the *ortho* states only), finally the (+) or (−) in parentheses indicates symmetric or antisymmetric tunneling-inversion symmetry for the NH_3 subunit.

Symmetry	State	Angular contributions
A_2''	$\Sigma(0_0, n=0)$	$0.937\Sigma^+0_0^+(-)+0.034\Sigma^+1_0^+(+)+0.012\Sigma^+2_0^+(-)+0.010\Sigma^+3_3^+(-)$
A_2''	$\Pi(1_0, n=0)$	$0.960\Pi^+1_0^+(+)+0.016\Pi^+2_0^+(-)+0.016\Pi^-3_3^+(+)$
A_2''	$\Sigma(1_0, n=0)$	$0.703\Sigma^+1_0^+(+)+0.281\Sigma^+0_0^+(-)$
A_2''	$\Sigma(0_0, n=1)$	$0.659\Sigma^+0_0^+(-)+0.274\Sigma^+1_0^+(+)+0.032\Sigma^+2_0^+(-)+0.029\Sigma^+3_3^+(-)$
A_2''	$\Delta(2_0, n=0)$	$0.945\Delta^+2_0^+(-)+0.035\Delta^+3_3^-(-)$
E'	$\Sigma^s(1_1, n=0)$	$0.900\Sigma^+1_1(+)+0.036\Sigma^+2_2(+)+0.036\Pi^+1_1(+)+0.014\Sigma^+2_1(-)$
E'	$\Pi^{lower}(1_1, n=0)$	$0.506\Pi^+1_1(+)+0.422\Pi^-1_1(-)+0.035\Sigma^+1_1(+)$
E'	$\Pi^{upper}(1_1, n=0)$	$0.490\Pi^-1_1(-)+0.392\Pi^+1_1(+)+0.033\Pi^+2_1(-)+0.032\Pi^-2_1(+)$
E'	$\Sigma^s(1_1, n=1)$	$0.538\Sigma^+1_1(+)+0.341\Sigma^+2_2(+)+0.103\Sigma^+2_1(-)$
E'	$\Pi^{lower}(1_1, n=1)$	$0.346\Pi^+1_1(+)+0.213\Pi^+2_2(+)+0.175\Pi^-1_1(-)+0.144\Pi^-2_2(-)$
E'	$\Pi^{upper}(1_1, n=1)$	$0.394\Pi^-1_1(-)+0.144\Pi^+1_1(+)+0.118\Pi^-2_2(-)+0.112\Pi^-2_1(+)+0.076\Pi^+2_1(-)$
E'	$\Pi^{lower}(2_1, n=0)$	$0.473\Pi^-2_1(+)+0.405\Pi^+2_1(-)+0.044\Pi^+2_2(+)+0.043\Pi^-2_2(-)$
E'	$\Sigma^a(2_1, n=0)$	$0.539\Sigma^+2_1(-)+0.109\Pi^-2_1(+)+0.086\Sigma^+1_1(+)+0.071\Pi^+2_1(-)$
E'	$\Pi^{upper}(2_1, n=0)$	$0.263\Pi^+2_1(-)+0.164\Pi^-2_1(+)+0.167\Sigma^+2_1(-)+0.096\Pi^+1_1(+)+0.093\Pi^-1_1(-)$

for a T-shaped configuration with the Ar localized in the half-plane that contains the NH_3 symmetry axis, and bisects the angle between two hydrogens. Expressed in our coordinate system, Bulski *et al.*[20] find the global minimum to be 134 cm^{-1} deep, located at $R=3.59$ Å, $\theta=105°$, and $\phi=60°$. Chałasiński *et al.*[19] find the global minimum to be 115 cm^{-1} deep, located at $R=3.76$ Å, $\theta=101°$, $\phi=60°$. Experimentally, we find the global minimum to be 149.6 cm^{-1} deep, located at $R=3.57$ Å, $\theta=96.6°$, and $\phi=60°$. The surface is a delicate balance of attractive and repulsive forces, both of which are largest in magnitude near the hydrogens and the lone pair of electrons, and it only takes a small shift in either the attractive or repulsive energy, or a slight change in the anisotropy for the minimum of the IPS to move significantly. Table VIII of Ref. 11 compares the observed $\Pi(1_0, n=0)$ and $\Sigma(1_0, n=0)$ bending energy levels, ground state dipole moment, and the quadrupole coupling constants in the ground state, $\Pi(1_0, n=0)$ state, and $\Sigma(1_0, n=0)$ state with calculated values from these surfaces. It is seen that the *ab initio* surfaces attain qualitative, but not quantitative agreement with experiment. The surface of Bulski *et al.*[20] performs somewhat better than that from Chałasiński *et al.*[19]

The attractive and repulsive contributions of the two *ab initio* surfaces are in good agreement with each other along $\phi=60°$, but the surface of Bulski *et al.*[20] find more repulsion and less attraction along $\phi=0°$, which leads to a larger amount of variation. A qualitative difference between both *ab initio* results and the experimentally determined IPS is found by comparing Fig. 1 of Ref. 20 with Fig. 6 (remembering that θ in our coordinate system is $180°-\theta$ in their's). We find more attraction and repulsion at $\theta=180°$ than at $\theta=0°$ for a given value of R, whereas they find the opposite. That is, we find that the lone pair exerts a larger influence on the Ar atom than does the gap between the three hydrogen atoms, whereas they find the opposite.

Bulski *et al.* find roughly 110 cm^{-1} of variation in the surface as a function of θ and ϕ with R fixed at 7.09 bohr (3.75 Å). The experimentally determined surface has only about 40 cm^{-1} of variation for the same center-of-mass separation. We do find, however, about 100 cm^{-1} of variation when R is fixed at 3.57 Å, the configuration that passes through the minimum for $\phi=60°$ (Fig. 2), but there is little dependence on ϕ. The *ab initio* study of Bulski *et al.* finds almost 90 cm^{-1} of variation as a function of ϕ at this center-of-mass separation when θ is chosen such that the Ar passes over the hydrogens. When taking a cut of the surface at fixed R, there is always the possibility of finding more variation in the potential energy than the molecule would experience in traversing the minimum energy path, especially when there is a significant amount of angular-radial coupling. It could be that some of the variation of the energy reported by Bulski *et al.* arises from this effect. The position of the global minimum is quite close to that determined experimentally, thus any deviations of the eigenvalues and eigenvectors calculated from their surface from those measured experimentally are probably due to the excess anisotropy in their *ab initio* surface.

The surface of Chałasiński *et al.* does not have quite as much variation as a function of θ and ϕ. It has roughly 70 cm^{-1} of overall variation as a function of θ and ϕ at 3.75 Å, and about 45 cm^{-1} of variation as a function of ϕ when the Ar is confined to passing over the hydrogens. Since the anisotropy of this surface seems to be closer to that determined experimentally, the fact that the center-of-mass separation for the global minimum is somewhat too large must adversely affect the agreement with experiment. One expects lower anisotropy at larger R since both attractive and repulsive contributions are decreasing, and much more anisotropy might be found at smaller distances. The *ab initio* studies perform reasonably well in regard to the position and depth of the global minimum, but they find significantly more anisotropy than is present in the experimentally determined surface.

Very recently, a third *ab initio* study of the Ar–NH_3 complex has been carried out by Tao and Klemperer.[45] This study utilized supermolecular calculations using Møller–Plesset perturbation theory up to fourth order (MP4), and a basis set that contains functions at the midpoint between the Ar atom and the NH_3 center of mass. They find very good

agreement with experiment, and state that the bond-centered basis functions, or bond functions, are very effective in determining the correlation energy, which is normally obtained through polarization functions, while allowing the basis set size to be kept at manageable levels. They find the global minimum to be 130.1 cm^{-1} deep at $R=3.628$ Å, $\theta=90°$, and $\phi=60°$, compared to the 149.6 cm^{-1} deep experimentally determined global minimum located at $R=3.57$ Å, $\theta=96.6°$, and $\phi=60°$. Although the calculated well depth is 20 cm^{-1} smaller than the experimental value, the anisotropy in the well depth of the radial minimum as a function of θ and ϕ is typically reproduced to within 5 cm^{-1}. The largest discrepancy occurs at $\theta=135°$, $\phi=60°$ where the calculated value is 30 cm^{-1} above the global minimum, compared to an experimental value of 22 cm^{-1}. This calculated surface is exceptional in that it agrees equally well with the experimental surface for both $\phi=60°$ and $\phi=0°$. Similarly, the absolute position of the radial minimum is slightly over estimated by about 0.04 Å, but the anisotropy as a function of θ and ϕ is typically reproduced to within 0.02 Å. The largest discrepancy again occurs at $\theta=135°$, $\phi=60°$ where the calculated value is 0.13 Å too large. While the calculated position and depth of the radial minimum are both slightly more anisotropic than the experimental surface, and the calculated surface is still not of spectroscopic accuracy, this surface is the best *ab initio* surface for Ar–NH_3 to date. Furthermore, it is the only one to correctly characterize the delicate balance of anisotropic attractive and repulsive forces. Finally, this same level of theory has also been used to determine the Ar–HF and Ar–H_2O intermolecular potential energy surfaces in very good agreement with experiment,[45] thereby suggesting that this may be a reliable, general method to treat weakly bound complexes.

It is also possible to compare the experimentally determined Ar–NH_3 IPS with the AW2 IPS determined for Ar–H_2O.[1] The most striking difference is the location of the global minimum. In both cases the minimum occurs for the roughly T-shaped configuration. For Ar–H_2O it is found when the Ar atom is in the plane of the water molecule, whereas for Ar–NH_3 it is in the half-plane that contains the symmetry axis but is between two hydrogens. In the case of Ar–H_2O,[1] the AW2 surface has a single minimum about 145 cm^{-1} deep at $R=3.64$ Å and $\theta=74.3°$ with a 26 cm^{-1} barrier to internal rotation through $\theta=0°$, and 17 cm^{-1} barrier through $\theta=180°$ when the Ar is in the plane of the H_2O. When the H_2O subunit is rotated by 90°, the surface has saddle point at $\theta=100°$, which is about 55 cm^{-1} above the global minimum, and develops a double minimum. The primary minimum is at $\theta=180°$, and is about 20 cm^{-1} higher than the global minimum, and the secondary minimum is an additional 10 cm^{-1} higher and is found at $\theta=0°$. The two minima correspond, in fact, to the positions of the barriers to in-plane rotation, indicating the strong preference for the coplanar configurations.

In the case of Ar–NH_3, there is a single minimum about 145 cm^{-1} deep when the Ar is between two hydrogens at $R=3.57$ Å and $\theta=96.6°$, and the barriers to rotation are about 50 and 40 cm^{-1} through $\theta=0°$ and $\theta=180°$, respectively, i.e., the minimum when $\phi=0°$ is 27 cm^{-1} higher than the global minimum. The barriers are larger than for Ar–H_2O, but the preferred direction in both cases is through the configuration with the hydrogens pointing away from the Ar. Furthermore, upon rotating the NH_3 by 60° to obtain the configuration that places the Ar atom in the half-plane that contains a hydrogen atom (analogous to that for Ar–H_2O in which all four atoms are coplanar), the surface does not develop a double minimum. Rather, the minimum shifts to $\theta=105.6°$, it becomes much broader, and the barriers to internal rotation are about 21 and 12 cm^{-1} through $\theta=0°$ and 180°, respectively. Also, the center-of-mass separation increases by about 0.26 Å in going from the minimum of the surface for $\phi=60°$ to $\phi=0°$; whereas in the case of Ar–H_2O, the radial minimum only shifts from 3.64 Å for the global minimum to about 3.58 Å for the minimum when the Ar is constrained to remain perpendicular to the H_2O plane.

In summary, the Ar–NH_3 IPS is somewhat more anisotropic than that for Ar–H_2O with respect to end–over–end motions of the molecular subunit (the θ coordinate), while the Ar–H_2O IPS is significantly more anisotropic with respect to rotations of the molecule about its symmetry axis (the ϕ coordinate). The NH_3 and H_2O subunits both spend more time in the region of $\theta>90°$ than in the region of $\theta<90°$, but it must be remembered that in both cases the subunit samples all values of θ and ϕ. In contrast to these differences in the anisotropic aspects of the Ar–NH_3 and Ar–H_2O IPS, the isotropic contributions to the surfaces, β_{00}, ϵ_{00}, and R_{00}^m are fairly similar. The β_{00} parameters are 3.48 and 3.57 $Å^{-1}$, the ϵ_{00} parameters are 119.8 and 118.2 cm^{-1}, and the R_{00}^m parameters are 3.79 and 3.61 Å for Ar–NH_3 and Ar–H_2O, respectively.

In addition to comparing the Ar–NH_3 IPS with either *ab initio* studies or the IPS of other vdW complexes, it is also possible to compare our results with other experimental studies of Ar–NH_3. In particular, van der Sanden *et al.* have very recently calculated the collisional rotational excitation cross sections of NH_3 with Ar using the AA1 IPS.[46] The excellent agreement with the experimental cross sections[17] provides convincing proof that high-resolution (better than 1 MHz) spectroscopic studies can and do provide an accurate characterization of the IPS even in the repulsive regions of the surface accessed in the state of the art scattering experiments.

While it is possible to compare this multidimensional IPS with potential energy functions obtained previously,[11,12,14,16] it must be remembered that not explicitly treating the radial coordinate limits their ability to fully characterize the Ar–NH_3 complex. All of these approximate treatments find the nearly T-shaped configuration as the minimum energy, but they all significantly overestimate the energy difference between $\theta=0°$ and $\theta=180°$. The approximate treatments find the configuration with $\theta=180°$ to be more stable than that at $\theta=0°$ by 19 to 24 cm^{-1}, when the difference from the full multidimensional IPS is only 9 cm^{-1}. This example shows that while the approximate treatments correctly describe the gross features of the IPS, they cannot accurately describe the surface even in the angular coordinates due to the large amount of radial averaging. In fact, our previous investigations of Ar–H_2O have explicitly revealed the problems incurred in fitting experimental data to approxi-

TABLE XII. Position and depth of radial minimum along four directions in Ar–HF, Ar–H_2O, and Ar–NH_3. The difference between the quantities is also shown for $\theta=0°$ vs $\theta=180°$, and for the hydrogen bonded direction vs the antihydrogen bonded direction. The hydrogen bonded direction is indicated by Ar–HX, and the antihydrogen bonded direction by Ar–XH (X refers to F, O, or N).

X:	F	O	N
R_0^m (Å)	3.45	3.76	3.88
R_{180}^m (Å)	3.40	3.57	3.88
$\Delta R_{0,180}^m$ (Å)	0.05	0.19	0.00
ϵ_0 (cm^{-1})	217	119	100
ϵ_{180} (cm^{-1})	110	128	109
$\Delta\epsilon_{0,180}$ (cm^{-1})	107	−9	−9
R_{Ar-HX}^m (Å)	3.45	3.75	3.97
R_{Ar-XH}^m (Å)	3.40	3.48	3.56
$\Delta R_{Ar-H,Ar-X}^m$ (Å)	0.05	0.27	0.41
ϵ_{Ar-HX} (cm^{-1})	217	137	109
ϵ_{Ar-XH} (cm^{-1})	110	133	146
$\Delta\epsilon_{Ar-X,Ar-X}$ (cm^{-1})	107	4	−37

mate surfaces: viz., subsets of the spectroscopic data (e.g., the *ortho* states of Ar–H_2O can indeed be fit well to a purely angular surface, whereas larger sets of data (e.g., including the *para* states of Ar–H_2O) clearly cannot. Such behavior cannot be anticipated *a priori*, and the only reliable route is therefore to employ the full dimensionality of the IPS in the spectroscopic analysis.

Finally, a brief comparison of periodic trends from Ar–HF to Ar–H_2O to Ar–NH_3 is made. Table XII summarizes the position and depth of the radial minimum along $\theta=0°$, $\theta=180°$, along the hydrogen bonded configuration, and along the antihydrogen bonded configuration. First, the differences between $\theta=0°$ and $\theta=180°$ are considered. For Ar–HF, the radial minimum along $\theta=0°$ (which is also the hydrogen bonded configuration) is over 100 cm^{-1} deeper than that along $\theta=180°$, but the position of the radial minimum shifts only negligibly. In Ar–H_2O the radial minimum along $\theta=180°$ is only 9 cm^{-1} deeper than along $\theta=0°$, but the distance of the radial minimum moves in considerably (0.19 Å). In Ar–NH_3 the radial minimum along $\theta=180°$ is only 9 cm^{-1} deeper than along $\theta=0°$, and there is essentially no difference of the position of the radial minimum between the two configurations. The atomic radius does not change appreciably in going from F to O to N, but the electronegativity does change substantially. The differences in depth and position of the radial minimum at $\theta=0°$ compared to $\theta=180°$ can be rationalized in terms of the electron withdrawing ability of the hydrogen atom from the fluorine, oxygen, or nitrogen atom by extending the arguments presented in Refs. 1 and 3. The Ar atom can approach the H_2O molecule more closely along the oxygen end compared to Ar approaching HF from the fluorine end because there are two hydrogens withdrawing electron density from the oxygen, which is also less electronegative than fluorine. In the case of Ar–NH_3, where there are three hydrogens withdrawing electron density, and the electronegativity of nitrogen is smaller still, it would be expected that the Ar could approach very closely along the nitrogen end of NH_3, but the lone pair of electrons directed along $\theta=180°$ prevents the Ar atom from approaching closer than along $\theta=0°$. In the case of Ar–H_2O, the two lone pairs of electrons are directed along roughly $\theta=125°$, which allows the Ar to approach along $\theta=180°$.

Another meaningful way to compare the molecules is to compare the differences between hydrogen bonded and antihydrogen bonded structures. The position of the radial minimum along the hydrogen bonded configuration increases far more rapidly than the H–X bond length in going from Ar–HF to Ar–H_2O to Ar–NH_3 ($r_{FH}=0.926$ Å, $r_{OH}=0.972$ Å, $r_{NH}=1.012$ Å). This again is attributed to the electron withdrawing effect of the hydrogens. In going from F to O to N, the hydrogens have a higher electron density, which increases their effective size, thus the steric repulsion felt by the Ar atom will be felt at increasingly larger distances as both the bond length and effective hydrogen radius increase.

For Ar–HF, the hydrogen bonded orientation ($\theta=0°$) is strongly favored energetically over the antihydrogen bonded one ($\theta=180°$), but the position of the radial minimum shifts only negligibly. In Ar–H_2O the position of the radial minimum is significantly smaller (0.27 Å) along the antihydrogen bonded configuration ($\theta=125°$, $\phi=0°$) compared to the hydrogen bonded one ($\theta=55°$, $\phi=0°$), and the two configurations have roughly the same energy. In Ar–NH_3, as in Ar–H_2O, the position of the radial minimum is significantly smaller along the antihydrogen bonded configuration ($\theta=111°$, $\phi=60°$) compared to the hydrogen bonded one ($\theta=69°$, $\phi=0°$), but the antihydrogen bonded configuration is strongly favored energetically (by 37 cm^{-1}). Here, the trends are affected by both the electron withdrawing capability of the hydrogen atoms, as well as the position of the lone pairs of electrons. In Ar–NH_3, the Ar can move in along the antihydrogen bonded configuration with negligible interaction with the lone pair, whereas in Ar–H_2O, when the Ar approaches along the antihydrogen bonded configuration, there is repulsion from the lone pairs, even though they are positioned out of the molecular plane.

The global minimum in Ar–NH_3 is quite close to the antihydrogen bonded configuration. The long-range attraction is along the N–H bond and along the direction of the lone pair, however. These results underscore the importance of considering repulsive contributions to the IPS at close range. The long-range behavior is correctly described by dispersion and induction, but repulsion dominates the shape of the IPS at the position of the global minimum. Lone pairs of electrons also make important contributions to the shape of the IPS for all three of these vdW dimers. Judging from these trends, the Ar–CH_4 molecule would be expected to have the global minimum with the Ar atom in the threefold hollow formed by three hydrogens, which is the *ab initio* result obtained by Szczęśniak *et al.*[43] using the same level of theory as used by Chałasiński *et al.*[19] for Ar–NH_3. More generally, it seems clear from these results that one must exercise considerable caution in attempting to relate structures of complexes deduced from microwave spectroscopy to the intermolecular potential energy surfaces.

C. Summary

The multidimensional IPS for Ar–NH_3 has been determined by a fit to experimental spectroscopic data. A param-

eterized surface, with 13 variable parameters, successfully reproduces 61 experimental observations from 20 VRT states and second virial coefficients. The global minimum of the IPS is 149.6 cm^{-1} deep, and occurs at $R=3.57$ Å, $\theta=96.6°$, and $\phi=60°$. That is, in a roughly T-shaped configuration with the Ar atom between two hydrogens. It must be emphasized that while there is a well defined minimum on the IPS, there is not a well defined structure for this molecule, and the NH_3 subunit is undergoing large amplitude hindered internal rotations within the complex, and is executing the inversion–tunneling motion in some of the VRT states. While approximate methods of treating the internal dynamics can give some insight into the types of dynamics in this molecule, and are an appropriate starting point when there is a limited amount of data available, the only way to correctly treat the highly coupled motions is to perform the full multidimensional calculation. In this work the 3 vdW coordinates (R,θ,ϕ) were treated explicitly, and the NH_3 subunit tunneling inversion has been treated adiabatically, resulting in a quasi four-dimensional surface. The interplay of anisotropy in the IPS, Coriolis interactions, NH_3 inversion tunneling, and degenerate NH_3 states (E states) leads to a complicated and informative far infrared vibration–rotation–tunneling (FIRVRT) spectrum. The IPS obtained here will serve as a valuable benchmark for more approximate methods for describing molecular interactions that are better suited for use in molecular dynamics simulations.

The FORTRAN subroutine used to define the AA1 IPS is available from the authors upon request.

ACKNOWLEDGMENTS

The authors are grateful to A. Grushow and K. R. Leopold for numerous helpful discussions and for making their data available to us prior to publication. We are also grateful to J. G. Loeser, G. C. M. van der Sanden, and A. van der Avoird for helpful discussions. This work was supported through the Experimental Physical Chemistry Program of the National Science Foundation (Grant No. CHE-9123335).

[1] R. C. Cohen and R. J. Saykally, J. Chem. Phys. **98**, 6007 (1993).
[2] H. Kreek and R. J. Le Roy, J. Chem. Phys. **63**, 338 (1975).
[3] J. M. Hutson, Annu. Rev. Phys. Chem. **41**, 123 (1990).
[4] J. M. Hutson, J. Phys. Chem. **96**, 4237 (1992).
[5] R. C. Cohen and R. J. Saykally, J. Phys. Chem. **94**, 7991 (1990).
[6] A. H. Narten and H. A. Levy, J. Chem. Phys. **55**, 2263 (1971).
[7] K. L. Busarow, R. C. Cohen, G. A. Blake, K. B. Laughlin, Y. T. Lee, and R. J. Saykally, J. Chem. Phys. **90**, 3937 (1989).
[8] A. H. Narten, J. Chem. Phys. **66**, 3117 (1977).
[9] J. G. Loeser, C. A. Schmuttenmaer, R. C. Cohen, M. J. Elrod, D. W. Steyert, R. J. Saykally, R. E. Bumgarner, and G. A. Blake, J. Chem. Phys. **97**, 4727 (1992).
[10] D. H. Gwo, M. Havenith, K. L. Busarow, R. C. Cohen, C. A. Schmuttenmaer, and R. J. Saykally, Mol. Phys. **71**, 453 (1990).
[11] C. A. Schmuttenmaer, R. C. Cohen, J. G. Loeser, and R. J. Saykally, J. Chem. Phys. **95**, 9 (1991).
[12] E. Zwart, H. Linnartz, W. L. Meerts, G. T. Fraser, D. D. Nelson, Jr., and W. Klemperer, J. Chem. Phys. **95**, 793 (1991).
[13] G. T. Fraser, D. D. Nelson, Jr., A. C. Charo, and W. Klemperer, J. Chem. Phys. **82**, 2535 (1985).
[14] D. D. Nelson, Jr., G. T. Fraser, K. I. Peterson, K. Zhao, W. Klemperer, F. J. Lovas, and R. D. Suenram, J. Chem. Phys. **85**, 5512 (1986).
[15] C. A. Schmuttenmaer, J. G. Loeser, and R. J. Saykally, J. Chem. Phys. **101**, 139 (1994).
[16] A. Grushow, W. A. Burns, S. W. Reeve, M. A. Dvorak, and K. R. Leopold, J. Chem. Phys. **100**, 2413 (1994).
[17] J. Schleipen, J. J. ter Meulen, G. C. M. van der Sanden, P. E. S. Wormer, and A. van der Avoird, Chem. Phys. **163**, 161 (1992).
[18] B. Schramm, E. Elias, L. Kern, Gh. Natour, A. Schmitt, and Ch. Weber, Ber. Bunsenges. Phys. Chem. **95**, 615 (1991).
[19] G. Chałasiński, S. M. Cybulski, M. M. Szczęśniak, and S. Scheiner, J. Chem. Phys. **91**, 7809 (1989).
[20] M. Bulski, P. E. S. Wormer, and A. van der Avoird, J. Chem. Phys. **94**, 491 (1991).
[21] J. W. I. van Bladel, A. van der Avoird, and P. E. S. Wormer, J. Phys. Chem. **95**, 5414 (1991).
[22] J. W. I. van Bladel, A. van der Avoird, and P. E. S. Wormer, J. Chem. Phys. **94**, 501 (1991).
[23] J. W. I. van Bladel, A. van der Avoird, and P. E. S. Wormer, Chem. Phys. **165**, 47 (1992).
[24] G. C. M. van der Sanden, P. E. S. Wormer, A. van der Avoird, J. Schleipen, and J. J. ter Meulen, J. Chem. Phys. **97**, 6460 (1992); **100**, 5393 (1994).
[25] W. Yang and A. C. Peet, Chem. Phys. Lett. **153**, 98 (1988).
[26] A. C. Peet and W. Yang, J. Chem. Phys. **90**, 1746 (1989).
[27] A. C. Peet and W. Yang, J. Chem. Phys. **91**, 6598 (1989).
[28] J. M. Hutson, J. Chem. Phys. **89**, 4550 (1988).
[29] E. A. Reinsch and W. Meyer, Phys. Rev. A **14**, 915 (1976).
[30] M. D. Marshall and J. S. Muenter, J. Mol. Spectrosc. **85**, 322 (1981).
[31] C. G. Gray and K. E. Gubbins, *Theory of Molecular Fluids* (Clarendon, Oxford, 1984), Vol. 1.
[32] Š. Urban, D. Papoušek, J. Kauppinen, K. Yamada, and G. Winnewisser, J. Mol. Spectrosc. **101**, 1 (1983).
[33] C. H. Townes and A. L. Schawlow, *Microwave Spectroscopy* (Dover, New York, 1975); G. Herzberg, *Infrared and Raman Spectra of Polyatomic Molecules* (Van Nostrand Reinhold, New York, 1945).
[34] P. E. S. Wormer and H. Hettema, J. Chem. Phys. **97**, 5592 (1992).
[35] R. C. Cohen, Ph.D. thesis, University of California, Berkeley (1991).
[36] J. M. Hutson, J. Chem. Phys. **92**, 157 (1990).
[37] P. R. Bunker, *Molecular Symmetry and Spectroscopy* (Academic, New York, 1979).
[38] D. H. Gwo, Ph.D. thesis, University of California, Berkeley (1989).
[39] R. J. Le Roy, J. S. Carley, and J. E. Grabenstetter, Faraday Discuss Chem. Soc. **62**, 169 (1977).
[40] D. M. Brink and G. R. Satchler, *Angular Momentum* (Clarendon, Oxford, 1968).
[41] D. O. Harris, G. G. Engerholm, and W. D. Gwinn, J. Chem. Phys. **43**, 1515 (1965).
[42] R. J. Le Roy and J. M. Hutson, J. Chem. Phys. **86**, 837 (1987).
[43] M. M. Szczęśniak, G. Chałasiński, and S. M. Cybulski, J. Chem. Phys. **96**, 463 (1992).
[44] R. C. Cohen and R. J. Saykally, J. Chem. Phys. **95**, 7891 (1991).
[45] F. M. Tao and W. Klemperer, J. Chem. Phys. (submitted).
[46] G. C. M. van der Sanden and A. van der Avoird (private communication).